

# Journal of Astronomical Telescopes, Instruments, and Systems

AstronomicalTelescopes.SPIEDigitalLibrary.org

## **High-efficiency UV/optical/NIR detectors for large aperture telescopes and UV explorer missions: development of and field observations with delta-doped arrays**

Shouleh Nikzad  
April D. Jewell  
Michael E. Hoenk  
Todd J. Jones  
John Hennessy  
Tim Goodsall  
Alexander G. Carver  
Charles Shapiro  
Samuel R. Cheng  
Erika T. Hamden  
Gillian Kyne  
D. Christopher Martin  
David Schiminovich  
Paul Scowen  
Kevin France  
Stephan McCandliss  
Roxana E. Lupu

Shouleh Nikzad, April D. Jewell, Michael E. Hoenk, Todd J. Jones, John Hennessy, Tim Goodsall, Alexander G. Carver, Charles Shapiro, Samuel R. Cheng, Erika T. Hamden, Gillian Kyne, D. Christopher Martin, David Schiminovich, Paul Scowen, Kevin France, Stephan McCandliss, Roxana E. Lupu, "High-efficiency UV/optical/NIR detectors for large aperture telescopes and UV explorer missions: development of and field observations with delta-doped arrays," *J. Astron. Telesc. Instrum. Syst.* 3(3), 036002 (2017), doi: 10.1117/1.JATIS.3.3.036002.

**SPIE.**

# High-efficiency UV/optical/NIR detectors for large aperture telescopes and UV explorer missions: development of and field observations with delta-doped arrays

Shouleh Nikzad,<sup>a,\*</sup> April D. Jewell,<sup>a</sup> Michael E. Hoenk,<sup>a</sup> Todd J. Jones,<sup>a</sup> John Hennessy,<sup>a</sup> Tim Goodsall,<sup>a</sup> Alexander G. Carver,<sup>a</sup> Charles Shapiro,<sup>a</sup> Samuel R. Cheng,<sup>a</sup> Erika T. Hamden,<sup>b</sup> Gillian Kyne,<sup>b</sup> D. Christopher Martin,<sup>b</sup> David Schiminovich,<sup>c</sup> Paul Scowen,<sup>d</sup> Kevin France,<sup>e</sup> Stephan McCandliss,<sup>f</sup> and Roxana E. Lupu<sup>g</sup>

<sup>a</sup>Jet Propulsion Laboratory, California Institute of Technology, Pasadena, California, United States

<sup>b</sup>California Institute of Technology, Department of Physics, Mathematics and Astronomy, Pasadena, California, United States

<sup>c</sup>Columbia University, Department of Astronomy, New York, New York, United States

<sup>d</sup>Arizona State University, School of Earth and Space Exploration, Tempe, Arizona, United States

<sup>e</sup>University of Colorado, Laboratory for Atmospheric and Space Physics, Boulder, Colorado, United States

<sup>f</sup>Johns Hopkins University, Department of Physics and Astronomy, Baltimore, Maryland, United States

<sup>g</sup>BAER Institute/NASA Ames Research Center, Moffett Field, California, United States

**Abstract.** Exciting concepts are under development for flagship, probe class, explorer class, and suborbital class NASA missions in the ultraviolet/optical spectral range. These missions will depend on high-performance silicon detector arrays being delivered affordably and in high numbers. To that end, we have advanced delta-doping technology to high-throughput and high-yield wafer-scale processing, encompassing a multitude of state-of-the-art silicon-based detector formats and designs. We have embarked on a number of field observations, instrument integrations, and independent evaluations of delta-doped arrays. We present recent data and innovations from JPL's Advanced Detectors and Systems Program, including two-dimensional doping technology, JPL's end-to-end postfabrication processing of high-performance UV/optical/NIR arrays and advanced coatings for detectors. While this paper is primarily intended to provide an overview of past work, developments are identified and discussed throughout. Additionally, we present examples of past, in-progress, and planned observations and deployments of delta-doped arrays. © 2017 Society of Photo-Optical Instrumentation Engineers (SPIE) [DOI: 10.1117/1.JATIS.3.3.036002]

Keywords: detectors; delta doping; superlattice doping; UV; two-dimensional doping; atomic layer deposition; coatings; deployment; quantum efficiency; solar-blind silicon; silicon.

Paper 16061 received Jan. 9, 2017; accepted for publication Jul. 25, 2017; published online Sep. 1, 2017.

## 1 Introduction

Four flagship mission concepts are now under study by the astrophysics and exoplanet community Science and Technology Definition Teams (STDTs). The STDTs have been charged by the Director of NASA's Astrophysics Division to provide reports that will inform the basis for the next Astrophysics Decadal Survey. Two of these mission concepts, the large ultraviolet/optical/infrared (LUVOIR) surveyor mission and habitable exoplanet imaging mission (HabEx), address the need for a successor to the scientific legacy established by the Hubble Space Telescope (HST) and the exciting opportunity to search for life as a follow on to Kepler's planet finding discoveries.

Studies have been ongoing that build on the work of the National Research Council's Decadal Survey for Astronomy and Astrophysics, *New Worlds, New Horizons*.<sup>1</sup> These studies have consistently set forth technology development goals aimed at: (1) enabling a future large aperture, UVOIR flagship mission as a successor to HST; and (2) increasing the scientific reach of

smaller missions. The Cosmic Origins Program Analysis Group (COPAG) is now evaluating and recommending technology investments toward these goals through Science Interest Groups (SIG)s and Technology Interest Groups (TIG)s, and the Exoplanet Program Analysis Group (ExoPAG) is also making their recommendations. In both of these scientific focus areas, single-photon counting and ultralow noise detectors are a priority. Furthermore, these recommendations set as a goal very large format (i.e., 100-megapixel to Gigapixel), high quantum efficiency (QE), UV-sensitive detectors. Additionally, the Association of Universities for Research in Astronomy (AURA) convened a group to evaluate a next generation flagship large UVOIR space telescope. Their recommendation for the High-Definition Space Telescope (HDST) includes ultralow noise and UV-sensitive detectors as highest priority technology, especially when produced cost-effectively and in high numbers. These recommendations from AURA, COPAG and Astro2010 reflect the new understanding of the scientific opportunities enabled by technological breakthroughs and large-scale detector fabrication.

\*Address all correspondence to: Shouleh Nikzad, E-mail: [Shouleh.Nikzad@jpl.nasa.gov](mailto:Shouleh.Nikzad@jpl.nasa.gov)

Frontier astrophysical investigations are necessarily conducted at the limits of resolution, *étendue*, and sensitivity. A future 9- to 15-m UV/optical telescope mission will require significant detector advances beyond HST, Galaxy Evolution Explorer (GALEX), and Far Ultraviolet Spectroscopic Explorer (FUSE) detector technologies, particularly in QE, spectral responsivity in the UV, resolution, area, pixel count, and intrinsically low dark current. Dramatically increasing the efficiency of the detectors could allow explorer class or probe class missions to perform flagship mission science.

In this paper, we discuss our development of high-performance silicon detectors that are widely applicable to various UV/optical and UV missions in different classes from suborbital to orbital missions in explorer, probe, and flagship class missions such as LUVOIR or HabEx. Furthermore, we give an overview of the deployment of these detectors and discuss their potential future applications.

The development and deployment of delta-doped and superlattice-doped (also called “2D-doped,” as described in Sec. 3) silicon arrays is summarized pictorially in Fig. 1. Delta-doped arrays arose from efforts to address the surface passivation problems faced by the HST charge coupled devices (CCDs),<sup>2-5</sup> and the first delta-doped CCD was reported by Hoenk et al.<sup>6</sup> This first device was a 512 × 512 pixel EG&G Reticon CCD, which exhibited 100% internal QE, or reflection-limited response. Since then, 2D-doped, 12-Megapixel arrays have been demonstrated, JPL has developed end-to-end post-fabrication processing, JPL’s processing has been extended to wafer level, and device performance has been verified by various groups, including the group led by the Kepler PI for precision photometry.<sup>7</sup> Additionally, delta-doped arrays of various formats have successfully flown on multiple

suborbital flights, including sounding rockets with the University of Colorado, Johns Hopkins University, and Cornell/Dartmouth/Southwest Research Institute.

Delta-doped arrays have also been delivered for the Faint Intergalactic Redshifted Emission Balloon experiment-2 (FIREBall-2), a stratospheric balloon payload; and for the Colorado High-resolution Echelle Stellar Spectrograph (CHES), a sounding rocket payload. Recent and ongoing ground-based observations include work at Palomar Observatory and at Steward Observatory. Work completed during the past two decades has advanced the delta-doping technology such that it is perfectly poised to be incorporated into future explorer-class, probe-class, and flagship missions.

## 2 Scientific Detectors for NASA Missions

### 2.1 Silicon Detectors and Imaging Arrays

Silicon detectors and imaging arrays, especially CCDs and complementary metal oxide semiconductor (CMOS) arrays, are ubiquitous in different fields of imaging applications. This is due in part to the steady advancement of silicon Very Large-Scale Integration (VLSI) technology and the consumer market for imaging. Shortly after the invention of CCDs in 1969 at Bell Labs, extensive programs were established at JPL to advance early CCDs for imaging systems aboard NASA’s flagship mission Galileo<sup>8</sup> and its first great observatory, HST.<sup>5,9-11</sup> For an in-depth discussion of the history of CCDs and their use in space-based applications, we refer the reader to Janesick’s comprehensive *Scientific Charge-Coupled Devices*<sup>5</sup> and recent book chapter of Nikzad et al. “Digital Imaging for Planetary Exploration” in the *Handbook of Digital Imaging*.<sup>12</sup>

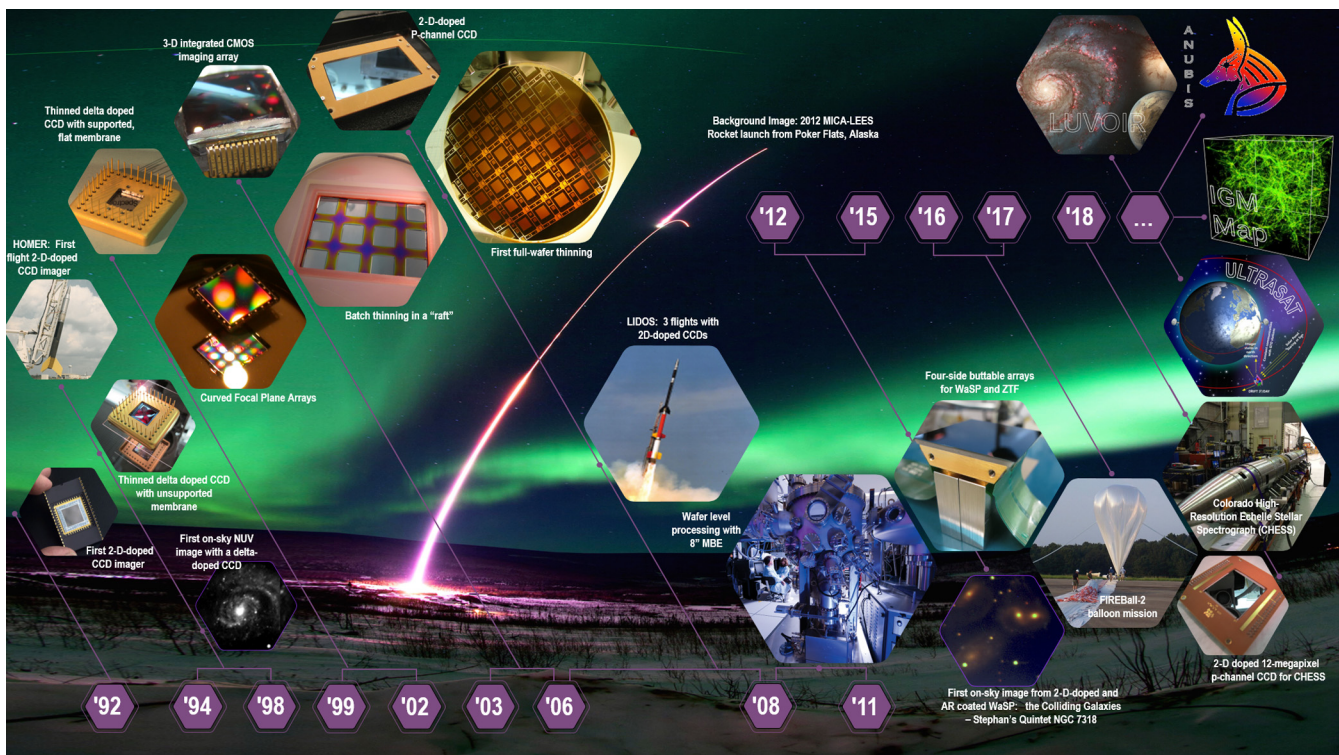


**Fig. 1** More than two decades of development and deployment have proven the capabilities and expanded the scale of delta-doped silicon arrays. This technology is well poised to make a significant impact on the capabilities of future explorer-class and flagship missions.

CMOS-based imaging started around the same time in the 1960s,<sup>13</sup> but it was not until the 1990s that its development began in earnest due in part to fabrication advancement and to focused efforts on CMOS-active pixel sensor development at JPL<sup>14,15</sup> and other CMOS imagers elsewhere. CMOS imaging has had an enormous impact on the consumer field and in recent years has become viable for scientific applications.

Through the years, the metrics of detector performance have progressed as VSLI technology has matured. Today, silicon

**Table 1** Summary of silicon-based device architectures and application considerations for each.

Detector	Description and considerations
CCDs	First digital imaging arrays in space, CCDs have characteristically linear response, high uniformity, and low noise. They are read out serially, which requires multiple charge transfer steps. Workhorse for scientific imaging. Wafer-scale production of scientific-grade detectors is possible
CMOS	Similar in concept to CCDs but with parallel readout enabled by “amplifier per pixel” capability. Highly driven by commercial applications, low-noise CMOS imaging arrays are becoming available for scientific applications. Parallel readout with per pixel amplifier allows for fast/versatile readout
High-purity silicon devices	CCDs made from high-purity/high-resistivity material. The entire silicon volume is depletable to 200 to 300 $\mu\text{m}$ depths. <sup>19</sup> As such, NIR ( $\lambda \sim 1 \mu\text{m}$ ) photons can be detected efficiently and without fringing, giving improved red response. Thinning to epitaxial thicknesses (5 to 15 $\mu\text{m}$ ) not required
EMCCD: electron multiplying CCD	“CCDs with gain.” An additional serial register, the “multiplication” or “gain” register. With a modest applied voltage (40 to 50 V) a gain of 1000s can be achieved. Essentially eliminates read noise. Single-photon counting capability. Can be operated in “normal mode” or in “photon counting mode,” effectively increasing the dynamic range of the detector
Hybrid arrays <sup>20–22</sup>	Detector circuitry and readout circuitry are fabricated in separate silicon wafers. These wafers are then physically/electrically interconnected; typically, with indium bump-bonding. Hybrid arrays combine high-sensitivity and fast readout capabilities. Detector and readout may be optimized independently
Low-noise CMOS	Also called “scientific” CMOS (sCMOS). Combines low-noise and robustness for space-based applications
APD: avalanche photodiode	Semiconductor version of a photomultiplier tube. High voltages (hundreds of volts) across the devices results in avalanche multiplication of charge
SPAD: single-photon counting avalanche diode	Reverse-bias PN avalanche diodes that operate in the Geiger mode to produce large current pulse; i.e., CMOS imager in which gain can be achieved within each pixel. <sup>23–25</sup> Single-photon counting capability and fast timing resolution ideal for time-resolved measurements

imagers are commercially available and cost far less than the developmental detectors that NASA funded for Galileo and HST. The imager array size has gone from  $800 \times 800$  (Galileo) to wafer-scale (e.g.,  $10 \text{ k} \times 10 \text{ k}$ ). At the same time, many other silicon detector technologies, including some that are capable of single-photon sensitivity, have been developed to meet the growing demand for high-performance, application-specific detectors (Table 1). While each of these device types differs in its architectural details, there is much overlap in terms of device physics underlying spectral sensitivity and dark current.<sup>16–18</sup> The processes described in this paper to passivate and stabilize the back surface leading to stable and high QE as well as extended spectral response (Sec. 3) are widely applicable to all silicon-based imaging arrays including the devices described in Table 1, as well as other silicon-based arrays.

## 2.2 Achieving High Quantum Efficiency and Extending Spectral Response in Silicon

The QE and spectral range of front-illuminated silicon detectors are limited by absorption and scattering by metals and polysilicon structures that form the essential circuitry on the front surface, regardless of the detector readout structure (e.g., CCD, CMOS, or APD). Very early in the history of silicon CCDs, it was realized that back-illumination offers an effective way to circumvent these limitations, potentially enabling broader spectral response and higher QE.<sup>2,3</sup> However, new limitations and technological challenges were immediately created by back illumination. Early back-illuminated detectors were plagued by time-variable and nonuniform back-surface charging, which resulted in severe problems with low, nonuniform, and unstable QE.<sup>4,5</sup> The severe quantum efficiency hysteresis (QEH) in WF/PC-1 CCDs launched an intensive R&D effort at JPL to develop a stable back-illuminated CCD. The history of JPL’s delta-doped CCD technology can be traced to the focused effort on solving the QEH problem.

Figure 2 shows a cross-section schematic drawing of the electronic band structure of a back-illuminated silicon imaging detector. The front surface electrodes are shown schematically on the right, and an oxide formed on the back surface is shown schematically on the left. Light enters through this thin oxide generating free charge carriers in the conduction band. In order to be detected, the charge carriers must move by drift and diffusion into the buried channel near the front surface. However, defects at the Si-SiO<sub>2</sub> interface create electronic states that can trap and release electrons and holes, resulting in time-variable surface charge and electric fields near the silicon surface. These fields can trap photogenerated charge, causing time-variable (unstable) QE; this is the source of QEH. Surface charging affects device performance at all wavelengths, but the shallow absorption depth of UV photons renders UV detectors especially vulnerable to surface defects and associated problems with low and unstable QE. Surface defects are also responsible for elevated surface-generated dark current, which introduces noise and reduces the sensitivity and dynamic range of scientific detectors.

In order to achieve stable, high QE in back-illuminated silicon detectors, and to reduce surface dark current, the surface must be passivated. However, the methods for passivation are constrained by the detector itself. Most surface passivation processes require high temperatures that would damage or destroy the detector. Several approaches have been developed to passivate and stabilize back-illuminated silicon detectors, including:

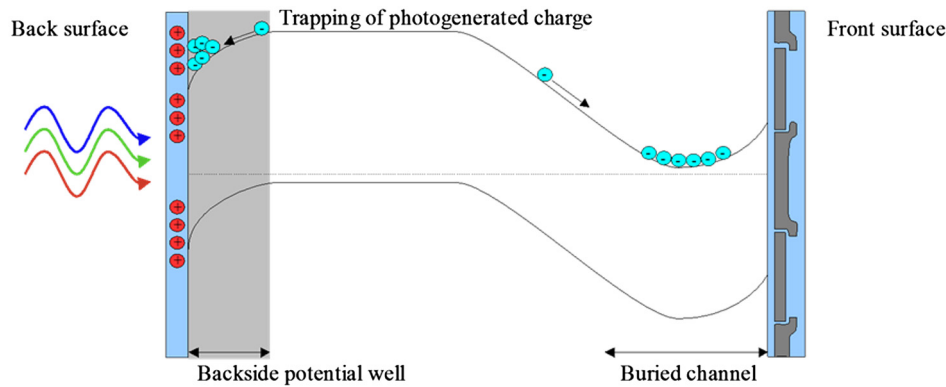


**Fig. 2** Schematic drawing of the electronic band structure in a back illuminated silicon imaging detector.<sup>26</sup>

1. Although not a surface passivation technique, the use of phosphorescent materials (e.g., coronene, lumogen) to down-convert UV photons to visible wavelengths was used as a “work around” to achieve UV sensitivity and improved QE.<sup>3</sup> This approach was used in the Wide-Field Planetary Camera on HST.<sup>4</sup> Although phosphorescent materials help to reduce the magnitude of the problem, they must be used in conjunction with backside charging or surface doping in order to eliminate QE entirely.
2. Backside charging methods (e.g., UV flood, flashgate, and/or chemisorption charging), which introduce net negative charge in the oxide to overcome any positive charge trapped in defects at the Si-SiO<sub>2</sub> interface. The main challenge for backside charging methods is one of stability, as dissipation of charge over time can necessitate the use of methods (e.g., a UV flood) to recharge the surface.<sup>27</sup>
3. Surface doping techniques, which stabilize the detector by reducing the thickness of the surface depletion layer and create an internal barrier that suppresses surface dark current.

JPL’s approach to surface passivation is based on a unique form of backside doping, which is described in detail in Sec. 3.

### 3 Delta-Doped Silicon Detectors

#### 3.1 Postfabrication Processing of Silicon Detectors

By using silicon-based detectors, the astrophysics, heliophysics, and planetary science communities are able to take advantage of the enormous investment made in the silicon industry. Even so, there are significant challenges to achieving high, stable QE spanning the UV/optical/NIR wavelength range, reducing the surface dark current, and achieving high-yield production of “science grade” devices. This section describes our development of postfabrication processing including delta doping and superlattice doping, which effectively and efficiently addresses these challenges and has been applied to a multitude of silicon array architecture and a high quantity of wafers and devices.

The photosensitive volume of most silicon detectors comprises a thin layer of high-purity epitaxial silicon that is grown on a thick, highly conductive silicon substrate. Highly conductive silicon makes a poor detector, as photogenerated

electrons are lost to recombination before they can be detected. In order to achieve high QE in a back illuminated detector, the thick substrate must be removed to expose the thin layer of high-purity silicon. Thinning a silicon detector to remove the substrate that is hundreds of microns thick, while leaving intact the 5- to 20- $\mu\text{m}$  silicon detector, proves to be extremely difficult. While early detectors were relatively small, the challenges of thinning have grown with the size of detectors. Even after the substrate has been removed, two essential problems remain. First and most obviously, the silicon substrate performs an essential function of mechanical support. An unsupported silicon detector is fragile and frequently deformed by internal stresses into a shape that has been compared with a potato chip. Second, the silicon substrate also performs an essential electrical function. Being electrically conductive, the silicon substrate forms a stable, equipotential surface, and functions as a back-surface electrode that prevents photo-generated charge carriers from causing transient voltage spikes at the back surface of the detector (also known as substrate bounce).<sup>5</sup>

#### 3.2 Backside Thinning

As previously discussed, backside illumination is required to achieve the best possible performance from silicon-based detectors. For backside-illuminated operation, all the excess silicon (i.e., the substrate) outside of the depletion region must be removed.<sup>28–31</sup> For conventional CCD and CMOS detectors, this requires thinning down to the epitaxial layer (5 to 20  $\mu\text{m}$ ); whereas for high-purity, fully depletable devices and APDs, for example, thinning to 200 to 300  $\mu\text{m}$  is sufficient.

Early detector thinning focused on “frame-thinning,” in which the thinned region is supported by the surrounding thick frame of silicon from the original full-thickness device. The process for frame-thinning involves a sequence of liquid etches that terminate at the epitaxial interface between bulk, low-resistivity silicon, and the high-resistivity silicon of the device’s epitaxial layer. With appropriate patterning techniques, the frame-thinning process can be carried out with a single detector, a raft of several detectors, or even an entire wafer (see Fig. 3). Frame-thinning offered a relatively fast approach to producing back-illuminated, thinned arrays; however, the approach produces fragile silicon membranes—sometimes as thin as 5  $\mu\text{m}$ —that tend to adopt a wrinkled shape [Fig. 3(a)] to accommodate the stress induced by the pixel structure.<sup>31</sup> Thus, the frame-thinning approach is not a sustainable approach for scaling up to large imaging arrays or high-throughput production of scientific imaging arrays.

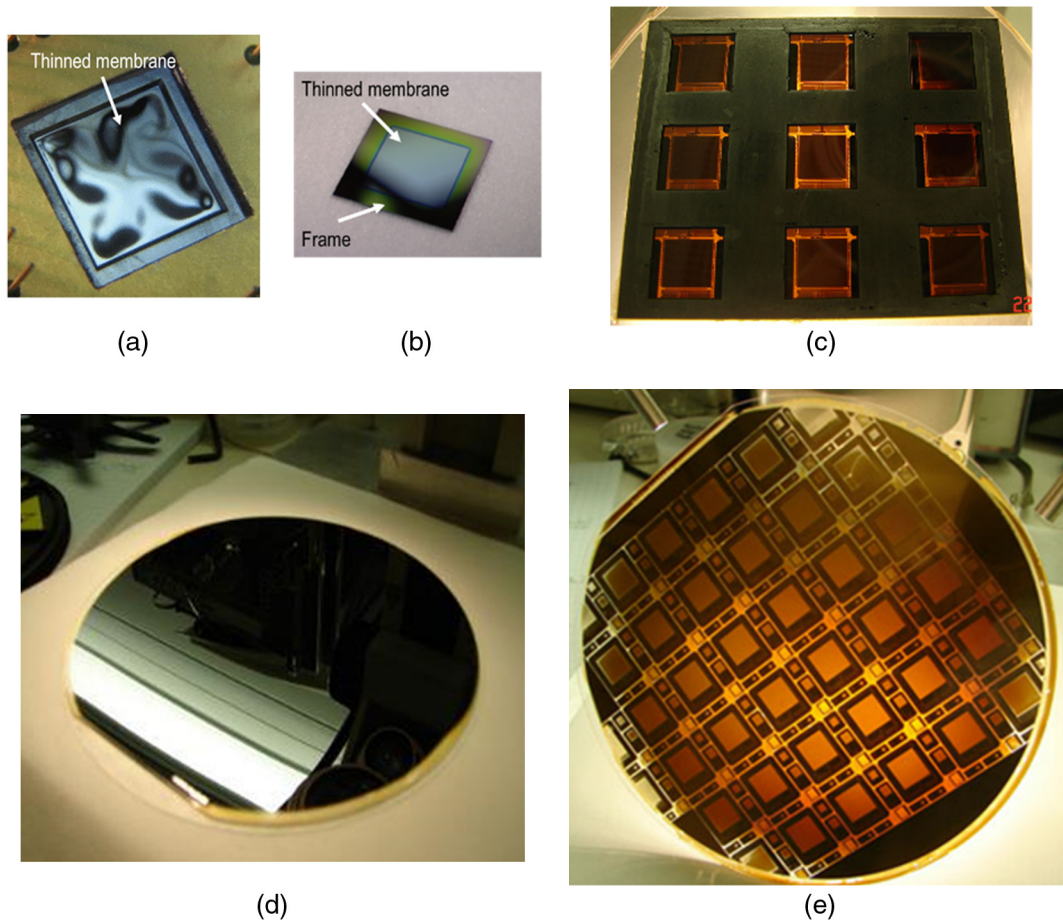


**Fig. 3** (a) A frame-thinned CCD with free-standing membrane. (b) A frame-thinned device with a supported membrane. (c) A frame-thinned, supported “raft” showing batch processing nine die that were thinned at once. (d) The backside of a bonded device wafer during the thinning process. (e) The backside of the same wafer thinned to  $5\ \mu\text{m}$ . In this case, the wafer is supported on a transparent quartz substrate; thus the entire structure is transparent.

A major advance came with the development of direct wafer-to-wafer oxide-bonding, in which two wafers are bonded together via the intermolecular forces between two very flat surfaces. In the case of the detector wafer, a thick oxide is added, patterned, and planarized. The device wafer front surface and that of a silicon support (or handle) wafer are activated by plasma etch, with the resulting surfaces each terminated with a labile bonding group.<sup>32</sup> The blank handle wafer serves (1) to protect the device wafer throughout the remaining processing steps and (2) as mechanical support for the thinned device wafer. Following the bonding step, the device wafer is thinned by grinding and chemical/mechanical polishing until the wafer thickness is reduced from hundreds of microns to tens of microns. The remainder of the substrate is removed by a selective thinning process, using a dopant-sensitive liquid etchant enabling the use of the epilayer as an etch stop. A final polish produces a mirror finish surface.<sup>33</sup> Using this wafer-level thinning process, thickness variations on the order of  $< 2\ \mu\text{m}$  can be achieved across an 8-in. wafer (Fig. 3).

It is important to note that the process of physically reducing the thickness of the silicon will affect the detector’s long wavelength response. Figure 4 shows the photon absorption length in silicon as well as the transmittance of silicon at varying thicknesses, including 10, 50, 200, and  $500\ \mu\text{m}$ ; from the plots it is clear that silicon becomes increasingly transparent as the

substrate is thinned, which will decrease red response. For cases in which high red response is needed, a fully-depleted, high-resistivity thick device should be used.

### 3.3 Silicon Passivation by Two-Dimensional Doping

As discussed in Sec. 2.2, back-illuminated detectors require surface passivation in order to achieve high, stable QE and reduce surface-generated dark current. Defects located at the Si/SiO<sub>2</sub> interface result in loss of efficiency and increased dark current. Because these effects are dynamic, they can make devices unstable, unreliable, and ultimately unusable. The goal of “surface passivation” is to create a stable, high-efficiency detector. One approach is to reduce the defect density and thereby reduce the charge density at the Si-SiO<sub>2</sub> interface. This approach played a key role in the history of the integrated circuits and silicon detectors. However, eliminating surface defects is not enough for a detector for at least two reasons. First, a detector needs to collect photogenerated charge, so it is necessary to engineer the surface to provide a stable, built-in electric field. Second, imaging detectors designed for use in the space environment must be able to withstand exposure to ionizing radiation. Ionizing radiation creates defects at the surface that can severely degrade detector performance (see Ref. 35 for data on EUV damage in ion-implanted CCDs). Of all of the approaches to

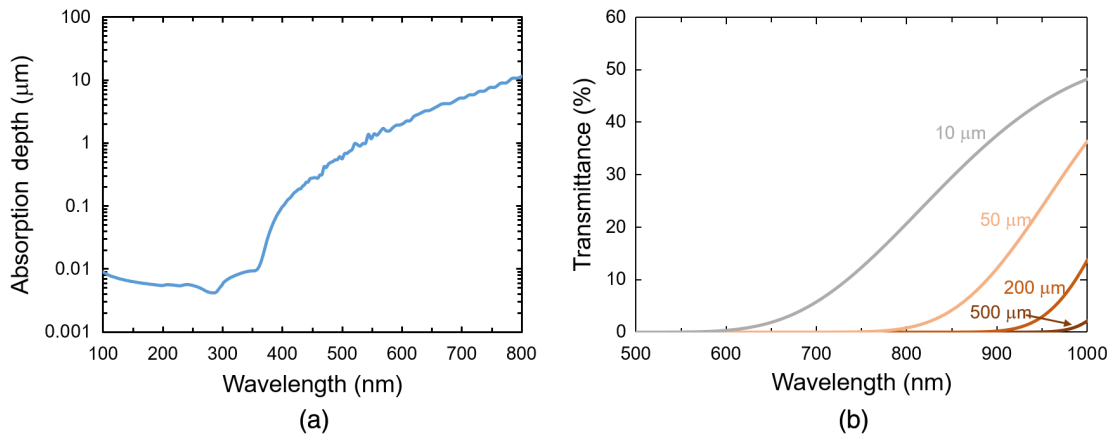


**Fig. 4** (a) Photon absorption length in silicon as a function of wavelength,<sup>34</sup> (b) Transmittance of silicon is plotted as a function of wavelength and for varying substrate thicknesses spanning 10 to 500  $\mu\text{m}$ .

surface passivation developed to date, none can match the sensitivity and stability of JPL’s delta- and superlattice-doping.<sup>26,36,37</sup>

Delta doping and superlattice doping are two-dimensional (2D)-doping techniques achieved by low-temperature molecular beam epitaxy (MBE).<sup>6,38–42</sup> The use of low-temperature MBE allows for control of the surface doping profile and band structure engineering with nearly atomic-scale precision. Furthermore, the low-temperature allows processing fully-fabricated devices. Conventional three-dimensional (3-D) doping processes produce random dopant distributions in the silicon lattice and are constrained by the solid solubility limit to a maximum achievable dopant concentration. For example, the solid-solubility limit for boron is approximately  $3.3 \times 10^{20}/\text{cm}^3$  at  $1100^\circ\text{C}$ .<sup>43</sup> Beyond this limit, dopant activation and crystalline quality are degraded. 2D-doping enables low-temperature crystalline growth of silicon with dopant concentrations at least an order of magnitude greater than this limit, while still achieving nearly 100% activation and high crystalline quality.<sup>44</sup> Atomic boron deposited by MBE on an atomically clean silicon surface

forms a self-organized, 2D phase with surface densities up to 0.5 monolayer ( $\sim 3.4 \times 10^{14}$  B/ $\text{cm}^2$  on a  $\langle 100 \rangle$  silicon surface). Subsequent growth of epitaxial silicon encapsulates and stabilizes this 2D layer of boron in the silicon lattice.<sup>45</sup> The process is termed “delta doping” because the resulting dopant profile resembles the mathematical delta function. “Superlattice doping” refers to a doping profile, in which more than one delta layer is incorporated into the MBE structure (Fig. 5).<sup>40</sup>

### 3.4 Optical Coatings Prepared by Atomic Layer Deposition

For low-light level applications, such as those described herein, it is critical to achieve the highest possible QE. JPL-invented 2D-doped silicon arrays exhibit 100% internal QE with their response following the reflection limit of silicon. Losses due to reflection can be significantly reduced through the use of antireflection (AR) coatings. Both hafnium oxide ( $\text{HfO}_2$ ) and aluminum oxide ( $\text{Al}_2\text{O}_3$ ) have been widely used as AR coatings with CCDs to improve visible QE (i.e.,  $\lambda > 400$  nm).<sup>46,47</sup>

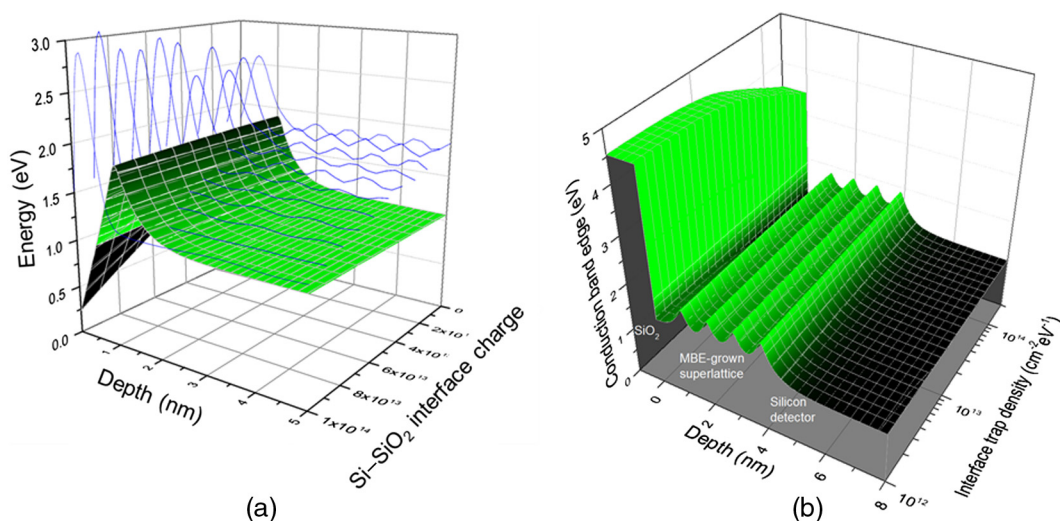


**Fig. 5** Plotted are the simulated band structure of (a) a delta-doped detector and (b) a superlattice-doped detector. 3-D surface plots show the conduction band energy (z-axis) as a function of depth from the Si-SiO<sub>2</sub> interface (x-axis), and interface trap density/charge (y-axis). The width of the surface potential well determined by the MBE layer structure. The blue traces in (a) show representative electron wavefunctions; quantum confinement effects increase the ground state energy and prevent trapping of photogenerated electrons at the 2D-doped surface.

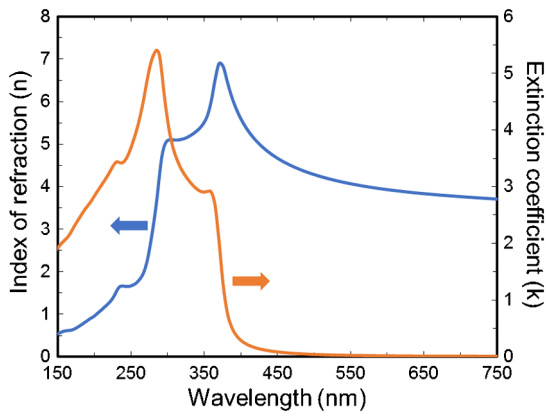


**Fig. 6** Optical properties of silicon, including the index of refraction (blue) and extinction coefficient (orange).

However, the rapidly varying optical properties of silicon in the UV wavelength range (Fig. 6) means there is no “one size fits all” AR coating for this challenging portion of the spectrum. Furthermore, most commonly-used AR-coating materials absorb far ultraviolet (FUV) light, and one is limited to FUV-transmitting materials, including several metal oxides ( $M_xO_y$ ) and metal fluorides ( $MF_2$ ).

Additionally, the uniformity of scientific imaging detectors is imperative; thus, it is critical that AR coatings also be uniform and pin-hole free. Atomic layer deposition (ALD) is a thin-film technique that utilizes a series of alternating, self-limiting chemical reactions at the substrate surface. ALD has been widely used for the preparation of a variety of materials, including the FUV-transmitting materials already mentioned.<sup>48</sup> During ALD, films are deposited one monolayer at a time; thus it is possible to produce ultrathin, highly conformal, stoichiometric films with high density and excellent uniformity. Furthermore, ALD allows for smooth surface morphology and stacked films with well-defined interface characteristics, as shown in the atomic force microscopy (AFM) and transmission electron microscopy (TEM) images in Fig. 7.

The AR coatings described above offer a well-established approach to improving detector response and can be tailored

for both broadband and narrow band performance. However, there are certain cases in which suppression of out-of-band light is desired. For example, the detection of faint UV signals is often hindered by inadequate rejection of background light in the visible and near infrared regions of the spectrum; this so-called “red-leak” in UV filters can mask the UV signal. HST’s WF/PC-II included two solar-blind Wood’s filters for red-leak suppression in the FUV.<sup>49</sup> These filters, which were fabricated at JPL, suppress visible light transmission to lower than  $10^{-8}$ . They comprise very thin layers of Na sandwiched between two  $MgF_2$  substrates. The challenge associated with Wood’s filters is that they are relatively unstable; the Na layer is quite reactive and tends to form pinholes over time, which will transmit in the visible. Furthermore, the in-band transmission is severely reduced by the Wood’s filter. Alternatively, UV instruments may employ in-line reflective optics (i.e., mirrors) with high in-band and suppressed out-of-band reflection. Using this approach, it is possible to reduce unwanted visible light to a few percent per reflection.<sup>50–52</sup> In order to achieve stable UV response together with high red-leak suppression, we turn to metal dielectric filters (MDFs) based on metal layers separated by transparent dielectric spacers. MDFs have long been used with transparent substrates for stand-alone filters, but only recently have we extended their use to silicon substrates for use as detector-integrated filters. Our initial proof of concept studies based on Al/ $Al_2O_3$  MDFs on bare silicon substrates (i.e., not device substrates) show excellent promise as UV band-pass filters, suggesting that it is possible to achieve high in-band QE with out-of-band suppression on the order of  $10^4$ . Compared to in-line transparent filters prepared on transparent substrates, on-chip filters allow for better index matching and higher in-band throughput [Fig. 8(a)].<sup>53</sup> We have recently extended our work to include Al/ $AlF_3$  filters; this work is published here for the first time. The use on  $AlF_3$  as the dielectric layer allows for greater flexibility in the position of the bandpass in the MDF [Fig. 8(b)] due to the lower short wavelength cutoff of  $AlF_3$ .

In addition to improved detectors, next-generation UV missions will require advancements in the realm of reflective optics, in particular improvements to the operating efficiency and environmental stability of standard Al mirrors. Additionally,

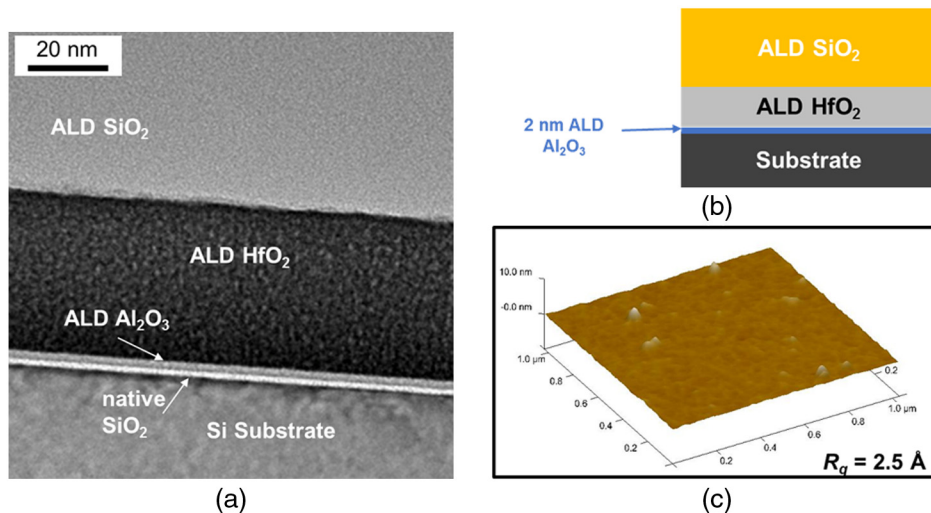


**Fig. 7** (a) TEM image of a stacked ALD films showing well-defined interfaces and uniform layers. (b) Schematic diagram of the coating shown in (a) and (c). (c) AFM image showing a  $1\text{-}\mu\text{m}^2$  region of the coating shown in (b). The surface roughness is  $\sim 2.5 \text{ \AA}$ , similar to that of the uncoated surface.

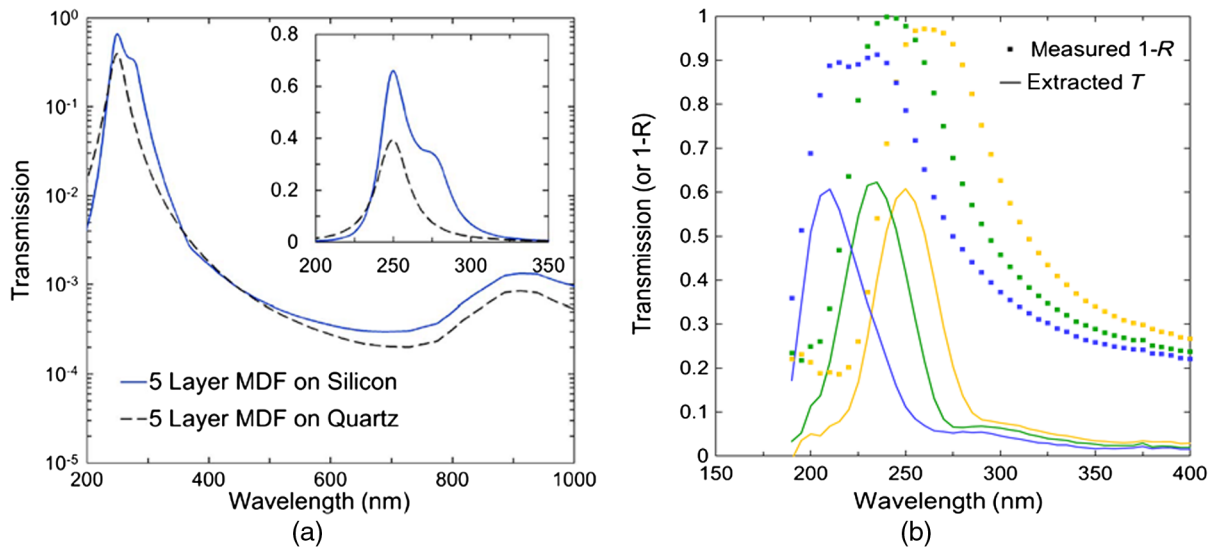


**Fig. 8** (a) Calculated performance of a five-layer MDF on silicon or quartz substrates. In band QE >60%, and out-of-band rejection approaches  $10^4$ .<sup>53</sup> (b) Prototype MDFs on Si using aluminum fluoride layers as an alternative to aluminum oxide with measured reflectance and projected transmittance based on ellipsometric characterization (not shown) for three designs optimized for 200 to 250 nm.

the high-efficiency cut-off will need to be pushed to shorter wavelengths, beyond what is available with conventional Al-MgF<sub>2</sub>. Extending the short-wavelength performance of conventional protected Al mirrors allows access to a rich spectral bandpass that has not been explored with high efficiency by previous NASA missions. The self-limiting nature of the ALD process makes it naturally scalable to large area substrates such as those envisioned for LUVOIR, and commercial systems have been demonstrated for the optical coating of meter-class substrates.<sup>54</sup> We refer the reader to our recent JATIS publication,<sup>55</sup> which describes our work in this arena and provides a potential roadmap for future developments.

The optical models presented in this paper were developed using the transfer matrix method and the TFCalc software package.<sup>56</sup> Optical constants for silicon, aluminum, and various metal oxides were taken from Palik and the Sopra database.<sup>56,57</sup> It is well known that a material's optical properties can vary depending on the deposition method; thus spectroscopic ellipsometry data collected using laboratory prepared samples (Horiba UVISSEL 2; J. A. Woollam VUV-VASE) were also used in modeling where appropriate.

### 3.5 Two-Dimensional Doping and End-to-End Processing of Different Device Architectures

JPL's standard postfabrication process as described above is summarized in Fig. 9.<sup>33,58</sup> Fully fabricated wafers are bonded to a handle wafer and back-thinned to the epi-layer. The wafer then undergoes several surface preparation steps to ready the surface for 2D-doping and optical coating processes. Finally, the back surface is patterned and etched to reveal bond pads prior to dicing and packaging.

Our standard processing steps can be modified/customized to accommodate the various device architectures described in Sec. 2.1. For example, the high-purity/high-resistivity devices can be fully depleted to a thickness of 200 to 300  $\mu\text{m}$ ; eliminating the need for a handle wafer as well as the need to thin to the epitaxial layer. Without the handle wafer, the front side electronics are exposed; however, it remains critical that the back surface is

atomically clean and ready for epitaxial growth prior to MBE. Thus, surface preparation techniques that avoid chemistries that would attack the existing circuitry must be used. Finally, the backside pattern and etch (i.e., pad opening) is not required with high-resistivity devices because the bond pads remain accessible from the front side. Similar modifications to the standard processes are made to accommodate APDs, hybridized arrays, and even front-side illuminated devices. Depending on the applications, we will implement our standard packaging or develop custom packaging as for example in the case of wafer-scale camera for prime (WaSP) closely butted devices described in Sec. 4.2.4.

### 3.6 Brief Overview of JPL's High-Throughput Processing Capabilities

Kepler's photometer is based on a 95-megapixel focal plane, comprised of an array of 42 CCDs; thus bringing us into the era of space-based extremely large focal plane arrays.<sup>59</sup> Data from the Kepler Space Telescope have expanded our view of the universe by increasing our awareness of the commonality of exoplanets and confirming the existence of 21 (as of publication) "Earth-like" planets within the habitable zone. ESA's GAIA, launched in 2013, utilizes 106 CCDs (comprising a nearly 1-gigapixel focal plane) in its mission to chart a 3-D map of the Milky Way and reveal the composition, formation, and evolution of our galactic neighborhood.<sup>60</sup> Future missions will utilize even larger focal planes based on mosaicked arrays or monolithic devices.

State-of-the-art CCD fabrication facilities currently use 6-in. wafers, and state-of-the-art CMOS imager foundries use 8-in. wafers. In order to enable full wafer scale production and batch processing of 2D-doped detectors, JPL developed infrastructure that includes acquiring a production-grade Veeco GEN200 Silicon MBE. This machine is equipped with a cluster tool with an automated sample transfer system that moves wafer platens between chambers under computer control. Attached modules include a load-lock chamber and an ultrahigh vacuum storage area with motorized elevators, enabling the loading and storage of up to eight wafer platens each for batch processing. Each 10-in. platen can be configured for single wafers up to 8 in.

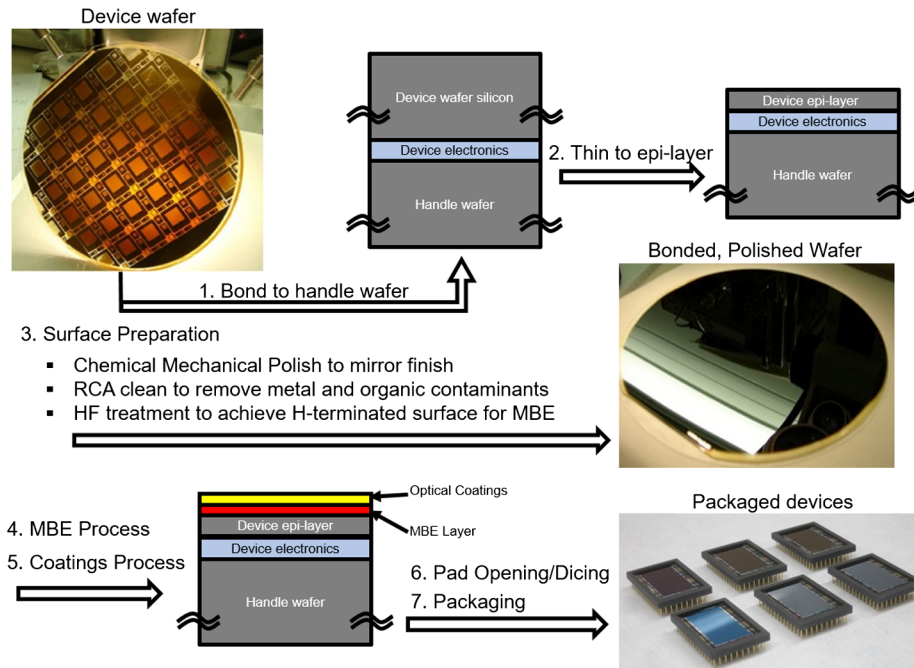


**Fig. 9** JPL's end-to-end postfabrication process flow to produce high-performance UV/optical/NIR sensitized devices with 100% internal QE and tailorable external QE.<sup>33</sup>

in diameter or for multiple smaller wafers. The preparation chamber is differentially pumped and equipped with a sample heater, gas inlet ports, and an RF source configured for implementing *in vacuo* surface preparation processes. The growth chamber has 12 effusion cell ports to accommodate multiple dopant materials, and dual e-beam sources enabling codeposition of silicon and up to four additional source materials. The entire system is under computer control, enabling the development of automated high-throughput, multiwafer processing.

Similarly, JPL's facilities include two ALD systems, both of which are capable of handling wafers up to 8 in. in diameter. The Beneq TFS 200 ALD System is a high-throughput, load-locked instrument. The growth chamber is equipped with inputs for six metal precursors, four reactive process gases, and two thermal reactive sources; also included is a specialized input for "challenging" precursors (e.g., small quantities or low stability) for R&D purposes. Additionally, the Beneq is equipped with an exchangeable chamber and gas distribution unit; thus, chambers can be project or process specific, which will minimize contamination. The small volume of the growth chamber allows for highly precise temperature control, and the plasma source in the Beneq ALD is fully configurable, offering direct and remote plasma process capability. The Oxford OpAL ALD System has a growth chamber equipped with inputs for up to three precursor compounds and six ports for reactive gases such as ammonia and hydrogen. In addition to the growth chamber, there is an integrated sample introduction glovebox that can hold and store multiple samples under dry nitrogen.

A more detailed paper is under preparation that quantitatively discusses the throughput on a variety of devices.

#### 4 Examples of Deployment of Two-Dimensional-Doped Silicon Arrays

Previous publications and their references have detailed the performance of 2D-doped arrays and have compared the response

of these detectors to relevant and previously-flown detectors. For example, Nikzad et al.<sup>30</sup> compared the response of delta-doped Loral and delta-doped EG&G Reticon CCDs to the performance of WF/PC II CCDs; these measurements were performed using the WF/PC II calibration setup. Similarly, Nikzad et al.<sup>61</sup> compared the QE of delta-doped and AR-coated conventional CCDs and EMCCDs with GALEX microchannel plate detector (MCP) data (also see Fig. 24). Additional publications further describe the high performance of delta-doped arrays in terms of uniformity of response, stability, and dark current.<sup>5,7,39,62</sup>

Typically dark current is improved with 2D processes as seen in the work by Blacksberg et al.,<sup>41</sup> which shows the lowest dark current measured in the LBNL p-channel CCDs. EG&G Reticon reported that delta doping improved the dark current performance compared with the standard UV-flood process for the same type of CCD. Spatial uniformity of dark current and QE are addressed in Janesick's book (Chapter 3).<sup>5</sup> Finally, Blacksberg et al.,<sup>63</sup> Greer et al.,<sup>64</sup> and Hoenk et al.<sup>39</sup> discussed the high stability and durability of AR-coated, 2D-doped CCD, and CMOS arrays.

The next steps of evaluation have taken 2D-doped devices beyond laboratory setups and into deployable systems. This section will describe the deployment of delta-doped and superlattice-doped arrays for suborbital and ground-based observations. We will also describe selected industrial applications and their relevance to NASA. Finally, we will describe several satellite missions currently under formulation that have baselined 2D-doped arrays.

#### 4.1 Deployments to Space via Suborbital Experiments

This section summarizes the suborbital flights of 2D-doped detectors processed in our laboratory, including delta-doped and superlattice-doped architectures. A summary of the devices to be discussed is given in Table 2.

**Table 2** Summary of completed and planned deployments of 2D-doped devices in suborbital payloads.

Mission	Device MFR	Device type	Pixel count	Pixel size ( $\mu\text{m}$ )
HOMER	EG&G	N-channel CCD	512 × 512	27 × 27
LIDOS	SITe	N-channel CCD	1100 × 330	24 × 24
MICA-LEES	Loral Fairchild	N-channel CCD	1024 × 1024	12 × 12
CHESS	LBNL-DALSA	High-purity p-channel CCD	3508 × 3512	10.5 × 10.5
FIREBall-2	e2v	EMCCD <sup>a</sup>	1024 × 2048 <sup>b</sup>	13 × 13

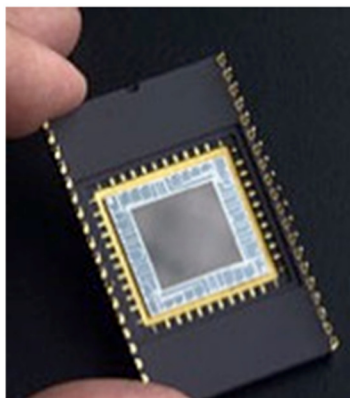
<sup>a</sup>N-channel.

<sup>b</sup>Commercially available CCD201-20 devices are typically operated in frame transfer mode with an image area of 1024 × 1024 active pixels.

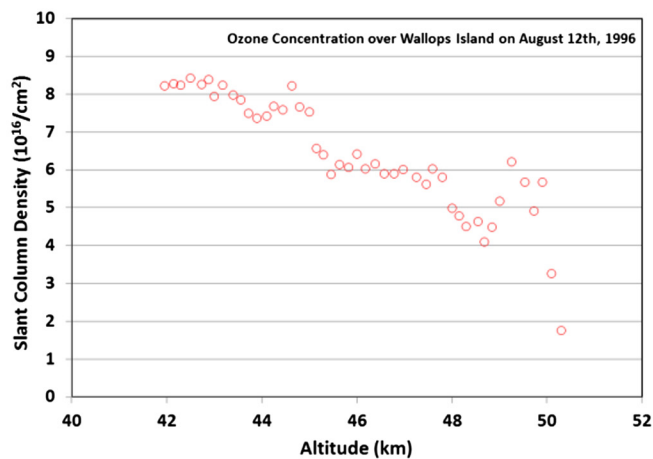
**4.1.1 HOMER: conventional N-channel CCD**

The High-altitude Ozone Measuring and Educational Rocket (HOMER; launched August 1996) was the third in a series of ozone-mapping rocket experiments managed by the Colorado Space Grant Consortium. Its primary objective was to determine the vertical distribution of the principle oxygen species related to ozone ( $\text{O}_3$ ) chemistry—including  $\text{O}_3$ , molecular oxygen ( $\text{O}_2$ ), atomic oxygen ( $\text{O}$ ), and nitric oxide ( $\text{NO}$ )—along the rocket

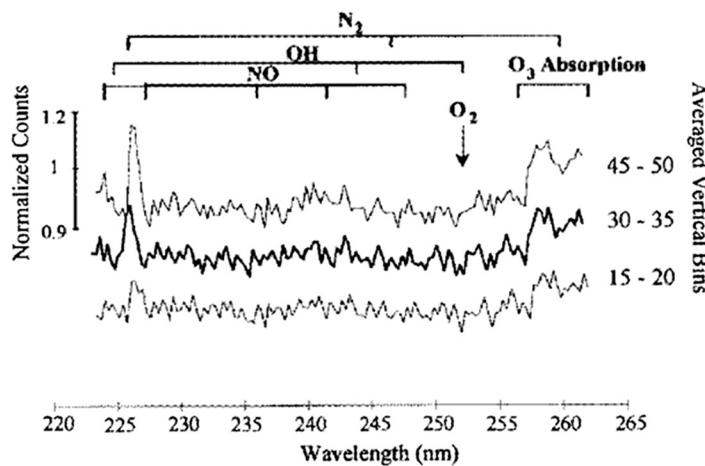
trajectory to obtain an understanding of the rate of  $\text{O}_3$  production as a function of altitude. In the first of the previous missions (1992), the Colorado Student Ozone and Atmospheric Rocket used photometers centered at 2680, 2959, and 4515 Å. For the second mission (1994), the Cooperative Student High-Altitude Rocket Payload added a spectrometer with a 512 × 512 pixel CCD detector. For the third flight, HOMER’s ultraviolet imaging spectrometer made measurements of the Earth’s limb in the FUV (215 to 265 nm) using a delta-doped CCD as the detector



(a)



(b)



(c)

**Fig. 10** (a) The HOMER detector, a 2D-doped 0.25-megapixel array. (b) Ozone concentration is shown as a function of altitude based on data returned from the HOMER mission. (c) UV airglow spectra of the Earth’s limb from HOMER.<sup>65</sup>

(Fig. 10). This early demonstration of the advanced UV sensitivity provided by delta doping successfully resulted in the measurement of the ozone column-concentration as a function of altitude. The delta-doped CCD was key to the success of the mission because of its ability to detect and spatially resolve the faint UV signal from atmospheric constituents.<sup>65</sup>

#### 4.1.2 LIDOS: conventional N-channel CCD

Two bare (i.e., no AR coating), rectangular ( $1100 \times 330$ ) delta-doped SiTe CCDs were delivered to Johns Hopkins University (JHU) for technology demonstration in the Long-slit Imaging Dual-Order Spectrograph (LIDOS). The delta-doped CCD was integrated into the LIDOS payload<sup>66</sup> and launched successfully aboard NASA sounding rocket missions 36.208 and 36.243.<sup>67,68</sup> Fixed exposure time observations were made of the UV-bright illuminating stars of the Trifid and Orion nebulae on the two flights. The detector is shown in Fig. 11(a). The spectrum of  $\theta^1$  Ori C (HD 37022) from the Orion nebulae mission (36.243) is shown in Fig. 11(b). The presence of a nonblack hydrogen absorption profile in the HI  $\lambda 1216$  transition, which is known to be highly saturated, suggests the presence of scattered visible light photons (red-leak) in the spectrograph. An MCP was also included in the payload and exhibited a perfectly black HI  $\lambda 1216$  profile for this object. A windowless lamp, which produces far-UV bremsstrahlung continuum and line emission from electron impact on a tungsten target and residual vacuum gases, was used to illuminate the long-slit of the

spectrograph to acquire simultaneous spectro/spatial flat fields of the two detectors. The comparison is shown in Fig. 11(c).

Based on these side-by-side comparison data, it was concluded that an ideal detector would combine the imaging performance and linearity of the CCD with the low background and photon counting ability of the MCP.<sup>67</sup> This work coincided well with the maturation of EMCCD technology and prompted our continued work toward the 2D-doped EMCCD, as discussed in further detail in Nikzad et al.<sup>33</sup> and Sec. 4.1.5. It should be pointed out that in most astronomical spectroscopic applications, the wavelength selectivity of the spectrometer and stand-alone filter combination removes the red leak and enables the use of silicon detectors. However, the final hurdle in using silicon detectors in the FUV is the development of solar-blind, UV bandpass filters, which is currently being addressed in ongoing work at JPL as discussed in Secs. 3.3 and 4.3.1 and Hennessy et al.<sup>53</sup>

#### 4.1.3 MICA-LEES: conventional N-channel CCD

The Magnetosphere-Ionosphere Coupling in the Alfvén Resonator (MICA) heliophysics sounding rocket mission incorporated a delta-doped array as the science detector in its low-energy electron spectrometer (LEES). The objective of this experiment was to investigate the role of active ionospheric feedback in the development of large amplitude/small-scale electromagnetic waves and density depletions in the low altitude (<400 km), downward current, auroral ionosphere—a critical component in understanding magnetosphere–ionosphere coupling.

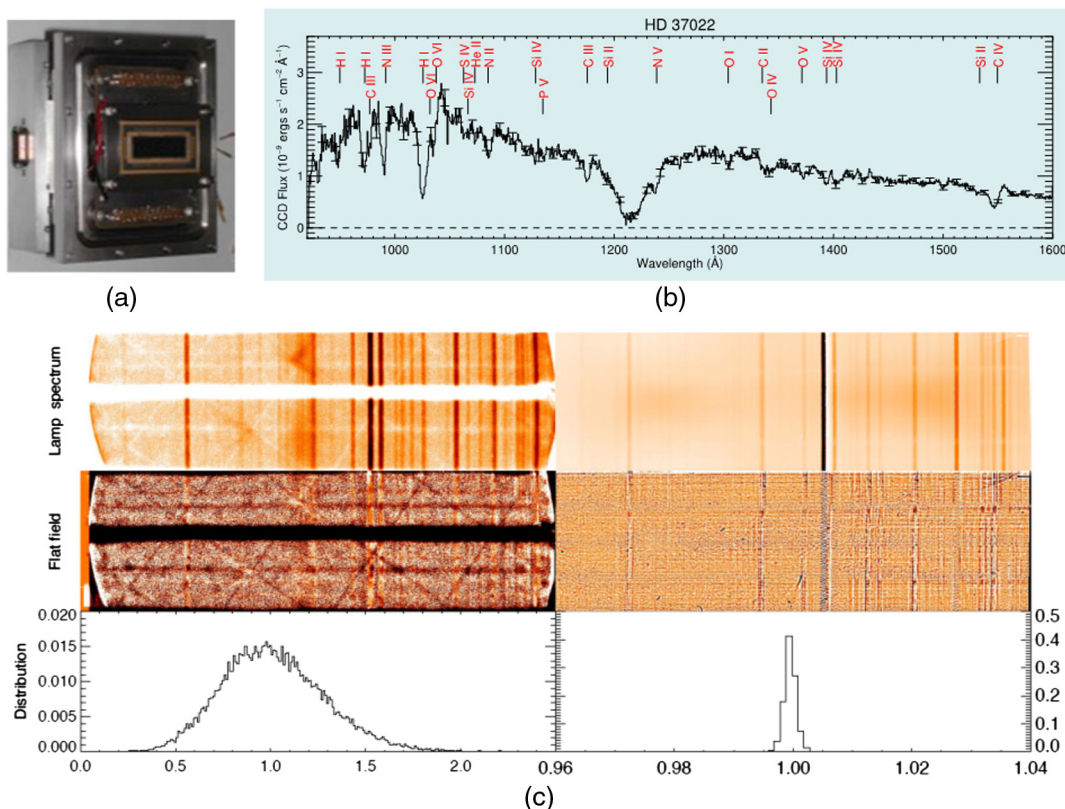


**Fig. 11** (a) Photograph of the delta-doped CCD in the payload. (b) Flight data from NASA/JHU 36.243 UG.<sup>67</sup> Far-UV spectra of the central OB star cluster of the Orion Nebula ( $\theta^1$  Ori C) were obtained with the LIDOS delta-doped array. These data are used to constrain the properties of dust and molecules in photodissociation regions.<sup>69</sup> (c) Spectrum of the electron-impact lamp mounted in front of the entrance aperture of the spectrograph and postprocessing flat fields for the MCP (left) and CCD (right) on board LIDOS. Histograms of the flat field variation are included at the bottom.

Delta-doped detectors allow direct detection of low-energy electrons without the need for high-voltage power supplies and can be used at lower altitudes than possible with conventional detectors (e.g., MCPs). For this application, we operated the imaging detector in “photodiode mode,” in which the entire output signal is added and read out as a current via a low-noise circuit, digitized, and stored. MICA had a successful launch with a functional LEES. The LEES experiment served the purpose of demonstrating the successful flight and operation of a delta-doped particle detector; see Fig. 12.

#### 4.1.4 CHESSE: high-purity P-channel CCD

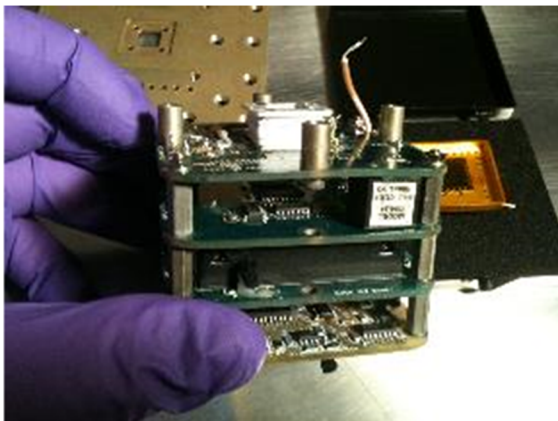
The CHESSE<sup>71,72</sup> is a rocket-borne far-ultraviolet spectrograph that serves as a pathfinder instrument and technology tested for high-resolution spectrographs for future NASA astrophysics missions (e.g., LUVOIR<sup>73</sup>). The CHESSE rocket experiment is designed to quantify the composition and physical state of the interstellar medium (ISM), specifically the interface regions between translucent clouds and the ambient diffuse ISM; quantifying the temperature, composition, and kinematics of nearby interstellar clouds. The local ISM provides an opportunity to study general ISM phenomena up close and in 3-D, including interactions of different phases of the ISM, cloud collisions,

cloud evolution, ionization structure, thermal balance, turbulent motions, etc. (see review by Redfield et al.<sup>74</sup>). The CHESSE instrument is an objective echelle spectrograph operating at  $f/12.4$  and resolving power of  $R \approx 120,000$  over a bandpass of 100 to 160 nm. CHESSE has flown successfully in 2014 and 2016 using a cross-strip anode MCP detector system; a description of the flight performance of the CHESSE instrument is provided in Hoadley et al.<sup>75</sup>

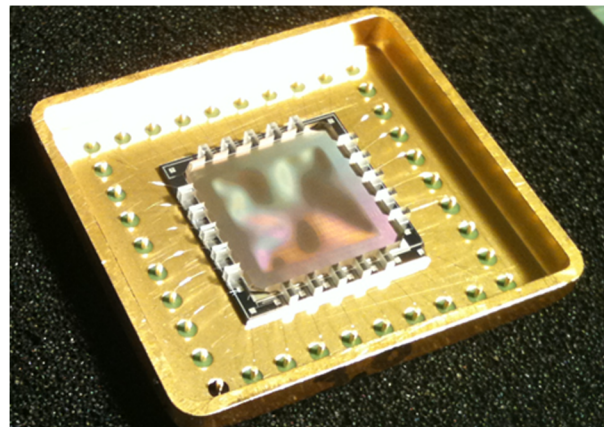
A future flight of CHESSE will incorporate an echelle grating fabricated using advanced electron-beam etching techniques developed at Pennsylvania State University, and the payload will be further reconfigured to replace the MCP detector with a delta-doped, SNAP CCD—a  $3508 \times 3512$  pixel,  $10.5\text{-}\mu\text{m}$  square pixel format, high-resistivity, p-channel CCD designed by Lawrence Berkeley National Laboratory (LBNL) (Fig. 13).<sup>19</sup> The devices are  $200\text{-}\mu\text{m}$  thick, back-illuminated, and packaged in a picture frame; because the CHESSE spectral range extends to 100 nm, the detector will be flown without an AR coating.

#### 4.1.5 FIREBall-2: EMCCD

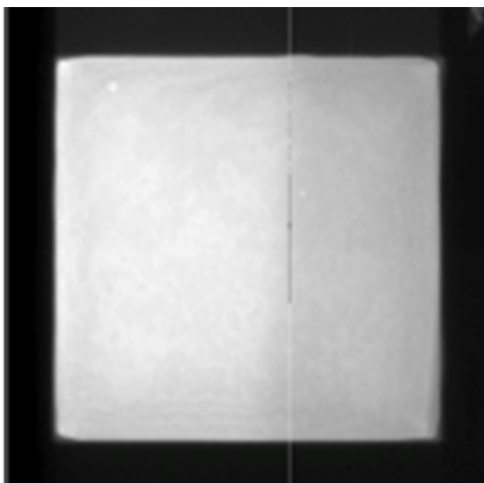
The Faint Intergalactic-medium Redshifted Emission Balloon (FIREBall-2) experiment is a balloon-born multiobject UV spectrograph designed to observe faint line emission from the



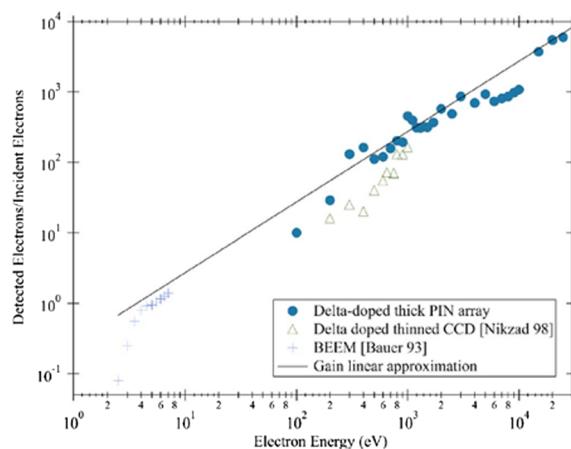
(a)



(b)



(c)



(d)

**Fig. 12** (a) MICA-LEES instrument and (b) photograph of the delta-doped CCD integrated into LEES. This device was produced early on with a front-side supported, frame-thinned membrane. (c) A “flat field” image taken with the device in response to protons and (d) a typical electron response of device.<sup>70</sup>

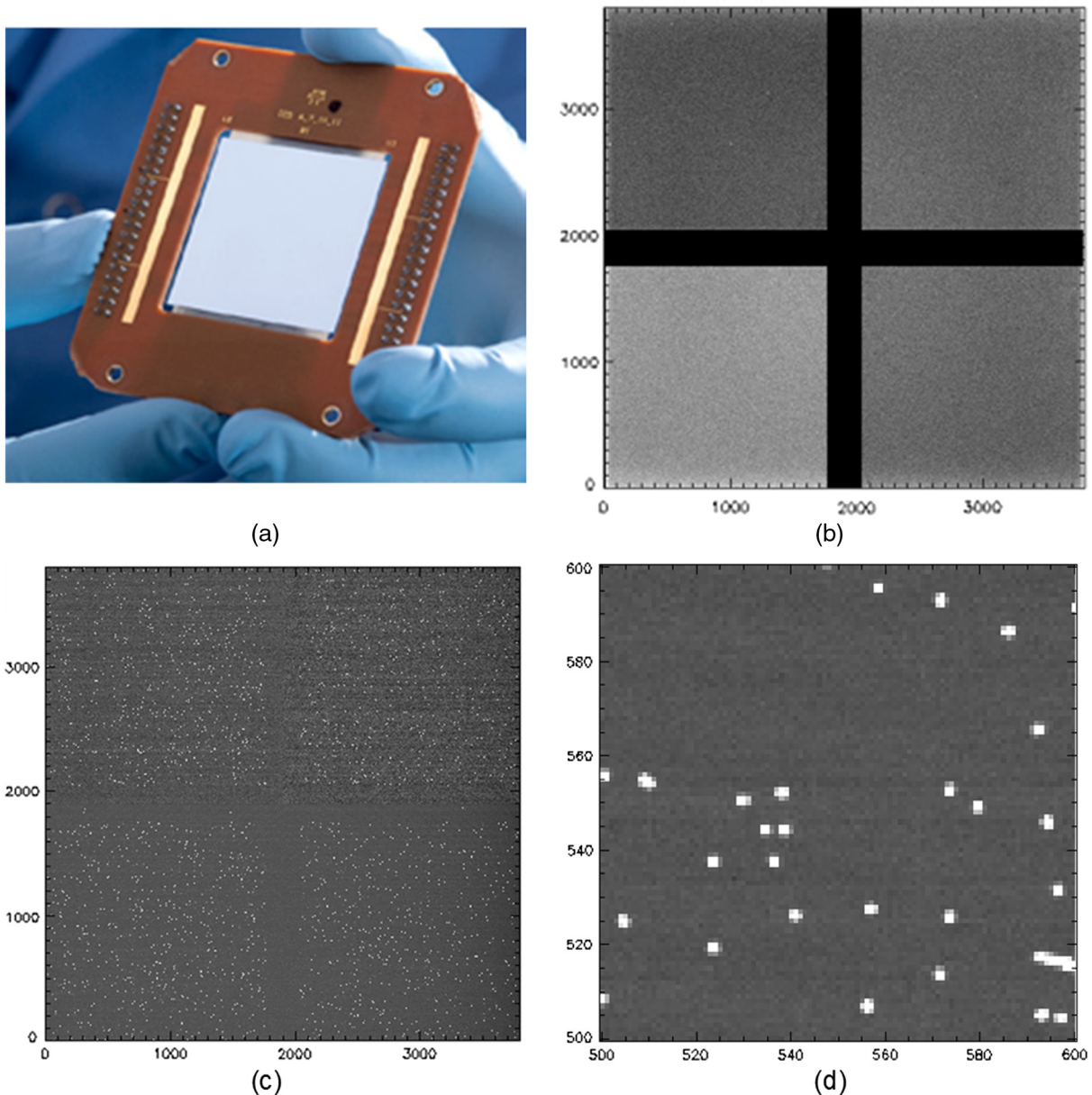


**Fig. 13** (a) A 2D-doped, p-channel (SNAP) CCD that will fly on a future iteration of CHESS. (b) A 500-nm flat field exposure (5 s,  $-140^{\circ}\text{C}$ ) with a 2D-doped SNAP CCD shows good uniformity. (c) x-ray measurements (20 s,  $-140^{\circ}\text{C}$ ) show excellent charge transfer efficiency (CTE). (d) A  $100 \times 100$ -pixel x-ray image from the same device. CTE for this device is  $\geq 0.999998$  in all quadrants.

circumgalactic media (CGM) of low redshift galaxies ( $z \sim 0.7$ ). A previous version of the FIREBall mission has flown twice, in 2006 and 2009.<sup>52,76</sup> The detector for FIREBall was a GALEX-near UV (NUV) spare MCP. FIREBall-2 will have improvements to the spectrograph that significantly increase the field of view, throughput, and number of targets per observation. These improvements will yield a factor of 30 increase in overall sensitivity allowing for multiple detections of the CGM in emission for the first time at UV wavelengths.

As a balloon-borne experiment operating in the upper atmosphere, FIREBall-2's UV operational range is limited to the stratospheric balloon window spanning  $\sim 195$  to 225 nm. Its detector is a 2D-doped and AR-coated EMCCD (e2v CCD201-20). Observations will be conducted using the EMCCD's photon-counting mode of operation, which will allow for detection

of the exceedingly faint signals to be observed. The commercially available CCD201-20 is operated in frame transfer mode with a total imaging area of  $1024 \times 1024$ ; however, for FIREBall-2, the customized device operates in full frame mode with an imaging area of  $1024 \times 2048$ . Here, we describe the development and performance of the AR coatings for FIREBall-2; for a more detailed account of device operation and performance, including photon-counting mode operation and dark current measurements, see Kyne et al.<sup>77</sup> Several AR coatings were considered for FIREBall-2, including single- and multiple-layer films. While multilayer AR coatings provide high QE with a narrow peak, variations in film thicknesses will result in a peak shift.<sup>78</sup> In the case of FIREBall-2, which is naturally constrained to a very narrow bandpass, we consider AR coatings with five or fewer layers with a broader bandpass that

encompasses the stratospheric window. Test coatings were prepared on test samples and functional test devices; test samples were evaluated in terms of their optical performance and related properties (e.g., surface and interface roughness) prior to moving to test devices. Transmittance data ( $100-R$ , %) from several of the FIREBall-2 coating development samples based on  $\text{Al}_2\text{O}_3$  and  $\text{SiO}_2$  are presented in Fig. 14, along with the predicted performance based on spectroscopic models. The single-layer AR coating (orange data points in Fig. 14) was applied to a FIREBall-2 device, which was incorporated with the spectrograph. Bench-top tests with a zinc source show that the device has good sensitivity in the 200- to 215-nm range, as expected. Additionally, read noise and dark current data show that the 2D-doping process is compatible with the EMCCD platform.<sup>77,79</sup>

## 4.2 Ground-Based Observations

This section summarizes the use of 2D-doped detectors at ground-based observatories; Table 3 provides a brief overview of the detectors that will be presented.

### 4.2.1 Palomar (I): conventional N-channel CCD

The first on-sky images of delta-doped CCDs provided rapid qualitative feedback from astronomer Jim McCarthy and team. A  $512 \times 512$ ,  $30\text{-}\mu\text{m}$  pixel, bare (i.e., no AR coating) delta-doped EG&G Reticon CCD was taken to Palomar Observatory for quick-look on-sky imaging in the near ultraviolet. Figure 15 shows two images of the same galaxy acquired in the (a) NUV taken by the delta-doped CCD and (b) the visible image from the Atlas. While there are some overlapping features, the UV image

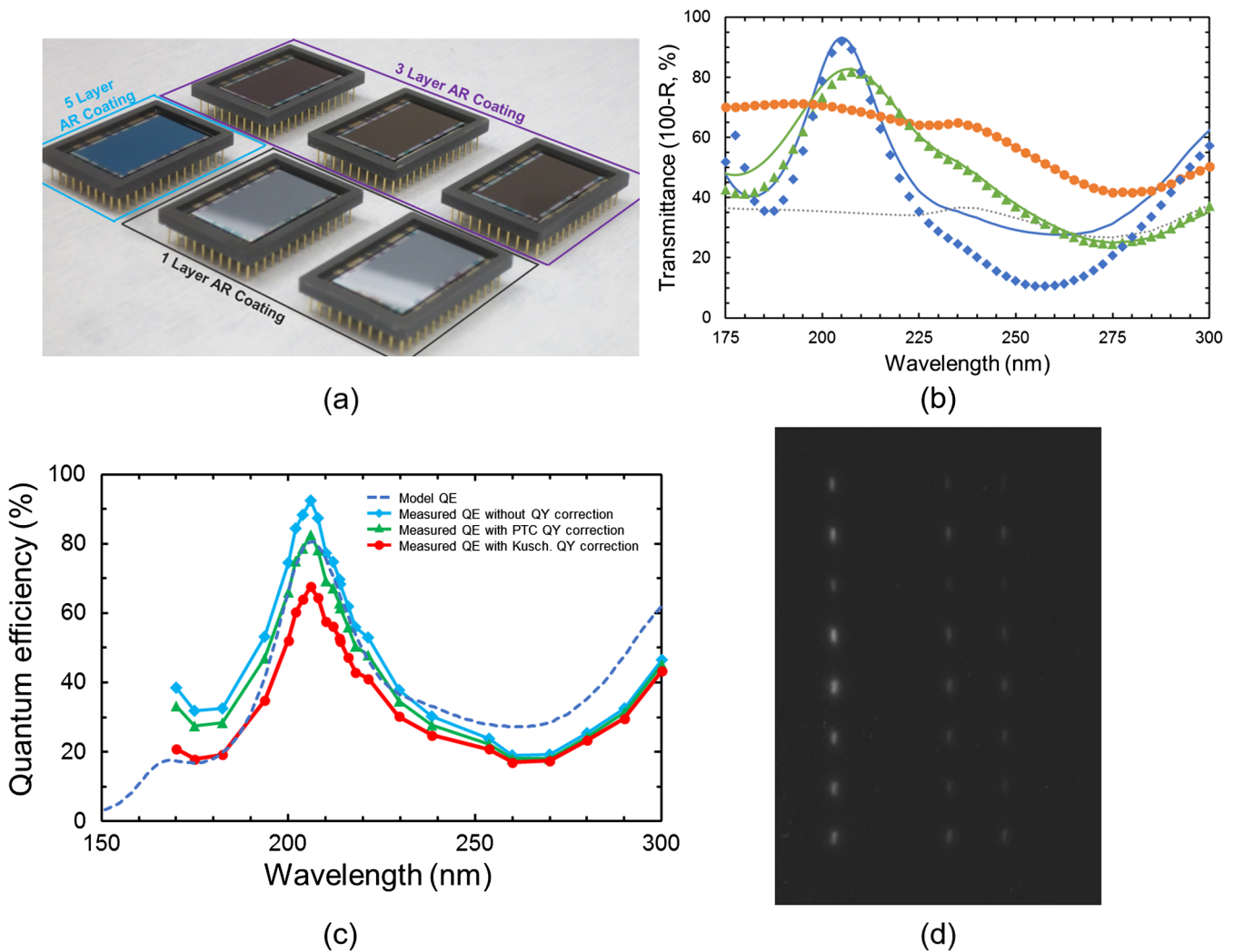


**Fig. 14** (a) Photograph of several 2D-doped CCD201 test devices for the FIREBall-2 project. These devices feature one-, three-, and five-layer AR coatings, distinguishable by their respective hues and labeling. (b) Model and measured transmittance ( $100-R$ ) for FIREBall-2 test samples (i.e., not test devices). Also shown is the reflection limit for bare silicon (dotted line). Both the models and transmittance are calculated based on reflectance ( $R$ ) and do not account for absorption within the film. (c) QE plot for a 2D-doped EMCCD with the five-layer FIREBall-2 AR coating. For comparison, we show the uncorrected QE measurement (blue) together with quantum yield (QY) corrected data. Two different QY corrections are shown: one determined by the photon transfer curve method (red), and one taken from literature (green).<sup>80</sup> This plot originally appeared in Ref. 81. (d) Zn line response (214, 206, 203 nm, left to right) on an optimized 2D-doped EMCCD in the FIREBall spectrograph.

**Table 3** Summary of completed and planned deployments of 2D-doped devices at ground-based observatories.

Observatory	Device MFR	Device type	Active pixels	Pixel size ( $\mu\text{m}$ )
Palomar (I)	EG&G Reticon	N-channel CCD	512 × 512	30 × 30
Lick	LBNL	High-purity P-channel CCD	2048 × 4096	2048 × 4096
Steward	LBNL-DALSA	High-purity P-channel CCD	3508 × 3512	10.5 × 10.5
Palomar (II)	STA	High-purity N-channel CCD	2064 × 2064	15 × 15
Palomar (III)	e2v	EMCCD <sup>a</sup>	1024 × 2048 <sup>b</sup>	13 × 13

<sup>a</sup>N-channel.

<sup>b</sup>Commercially available CCD201-20 devices are typically operated in frame transfer mode with an image area of 1024 × 1024 active pixels.

offers a more detailed view of the center of the galaxy and provides information about the hot surrounding areas. Specifically, in the UV, the younger hotter stars that form on the arm of the galaxy are easily distinguishable.

#### 4.2.2 Lick: high-purity P-channel CCD

A delta-doped, p-channel, 8-megapixel (2048 × 4096) LBNL CCD with high-broadband efficiency and high resolution

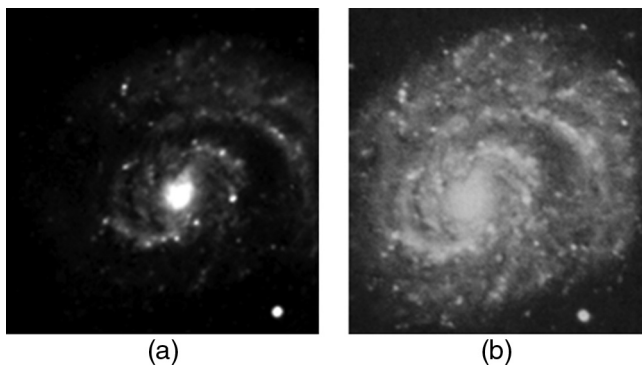


**Fig. 15** First on-sky images with a 512 × 512 delta-doped EG&G Reticon CCD in NUV. (a) Spiral galaxy 6137 imaged in the NUV (300 nm). (b) The same galaxy at imaged at visible wavelength (from astronomy Atlas).

(Fig. 16) was used for on-sky tests at Lick Observatory.<sup>63</sup> While this device sustained some damage during the integration in the dewar at the observatory, it was used to produce on-sky images such as those shown in Fig. 16.

#### 4.2.3 Steward: high-purity P-channel CCD

The CHESS flight prototype detector—a delta-doped, p-channel 3508 × 3512, 10.5- $\mu\text{m}$  pixel CCD (SNAP, LBNL)—was incorporated in the dewar at Arizona State University (ASU) and used for on-sky observation and quantitative analysis of the QE, etc. Figure 17 shows the images of astronomical objects during the expedition.

#### 4.2.4 Palomar (II): high-resistivity N-channel CCD

WaSP, a collaboration between Caltech Optical Observatories and JPL, is the new prime focus imager for the 200-in. telescope at Palomar Observatory, providing multiband color imaging from 320 to 1000 nm. WaSP was developed to replace the older large format camera with a single high-performance focal plane. Additionally, WaSP also serves as a technology pathfinder for the Zwicky transient facility (ZTF) on the 48-in. Oschin Telescope at Palomar, which will conduct high-cadence sky-surveys for transient astronomical objects. In order to achieve the highest image quality, the instrument needs dedicated guide and focus (G&F) CCDs to provide real-time

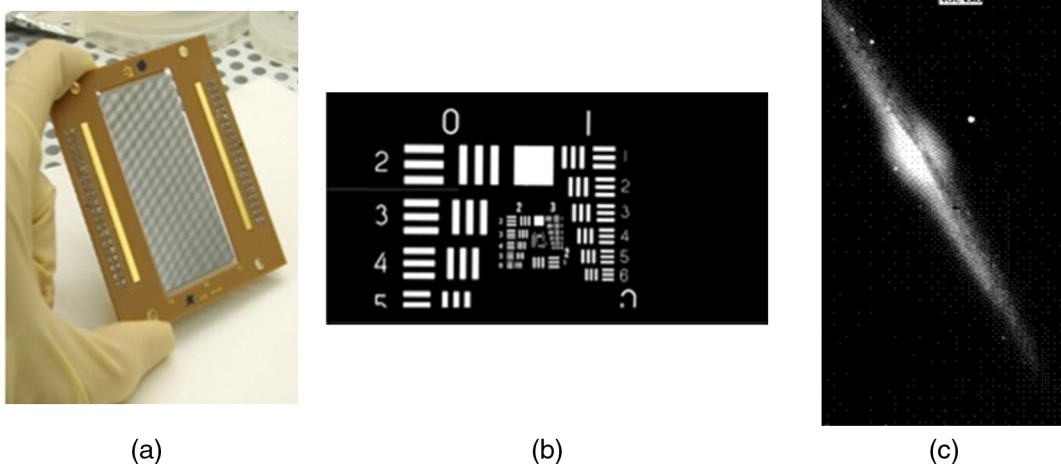


**Fig. 16** (a) Photograph of an 8-megapixel, 2D-doped, p-channel LBNL CCD. (b) A high-resolution pattern image with the same device. (c) First on-sky images with a 2D-doped, p-channel LBNL CCD (2048 × 4096).

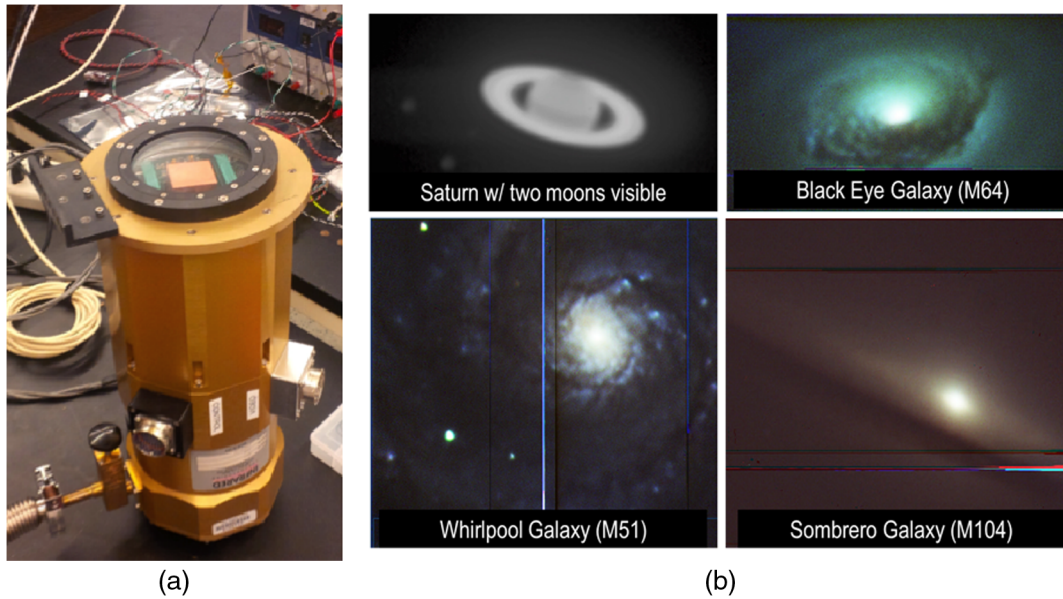


**Fig. 17** (a) An AR-coated version of the CHES prototype detector installed at Arizona State University and subsequently mounted on the back of the 61-in. Kuiper telescope at Steward Observatory. (b) First on-sky images with a 2D-doped and AR-coated SNAP CCD.

feedback to the telescope tracking systems and focus controls. The guide CCDs, in particular, need to have as high sensitivity as possible—especially in the U-band as they observe through the science filter. Additionally, due to the tight space constraints in the WaSP and ZTF dewars, the guide and focus CCDs needed to be positioned as close as possible to the main science CCD within each system. Here, we present the first overview discussion of the development of the G&F CCDs for WaSP and ZTF. A more in depth discussion of device operation and performance parameters will be the subject of future publications.

In response to these requirements of high-broadband sensitivity and close-proximity device mounting, JPL developed detectors based on the  $2064 \times 2064$ ,  $15\text{-}\mu\text{m}$  pixel format back-illuminated STA3600 CCD in a custom four-side buttable packaging. The STA3600 is a high resistivity, fully depleted

CCD developed by Semiconductor Technology Associates, Inc. (STA). The increased silicon thickness provides enhanced response at the red end of the visible spectrum, where the sensitivity of conventional thinned CCDs drops off rapidly. These devices were modified for UV-enhanced sensitivity using JPL's 2D-doping and AR coating technologies. The custom CCD package (shown in Fig. 18) reduces the detector footprint to the physical size of the detector die, with no wire-bonds or detector packaging projecting outside that area. The packaging requirements also called for meeting tight tolerances on the final package thickness, to avoid shimming (on a per detector basis) in the dewar to achieve focus. All CCDs (guide, focus and science) have been installed on a flexure mount in the correct focal plane positions. Device placement within the focal plane is repeatable to within  $20\ \mu\text{m}$  across multiple devices.

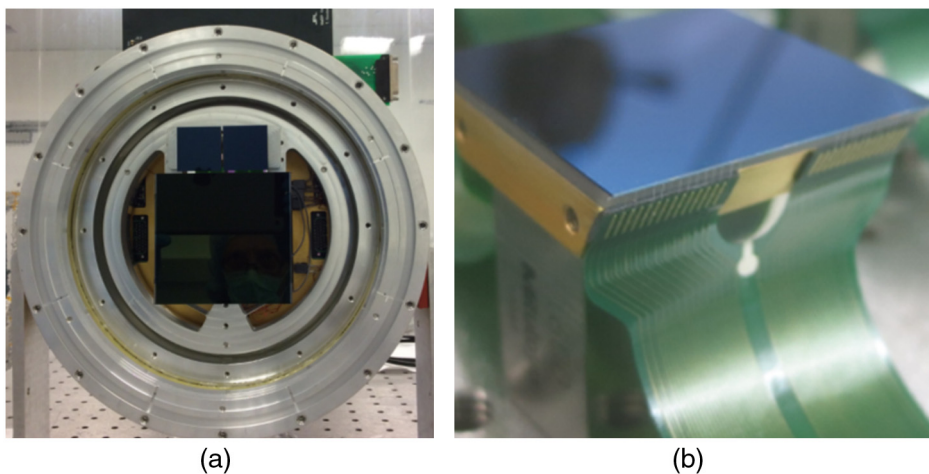


**Fig. 18** (a) The WaSP guide and focus CCDs installed in their dewar together with the science detector. The two 2D-doped and AR-coated parts are distinguishable by their blue hue. (b) A side view of one of the WaSP detectors showing the custom packaging, in which the support and flex cables to stay within the die footprint, allowing for four-side buttable mounting.

As previously mentioned, our collaborators on both WaSP and ZTF were particularly interested in improving performance in the U-band, but not at the loss of signal in the red. The AR coating development for WaSP, previously described,<sup>82</sup> was developed with this objective in mind. Designs with single- and multiple-layer films were developed based on  $\text{Al}_2\text{O}_3$ ,  $\text{HfO}_2$ ,  $\text{SiO}_2$ , and  $\text{TiO}_2$ . Test coatings were prepared on test samples as well as functional test devices; test samples were evaluated in terms of their optical performance and related properties (e.g., surface and interface roughness) prior to moving to test devices. Transmittance data ( $100-R$ , %) from several of the WaSP/ZTF coating development samples are presented in Fig. 19, along with the predicted performance based on spectroscopic models. Based on sample test data, design C was ultimately selected for WaSP/ZTF. Note that in cases where  $\text{HfO}_2$  was to be deposited directly onto the silicon surface, a 2-nm  $\text{Al}_2\text{O}_3$  diffusion barrier (d- $\text{Al}_2\text{O}_3$ ) was used in order to prevent an unfavorable chemical reaction between  $\text{HfO}_2$  and silicon.<sup>82,64</sup>

First light images from the WaSP guide and focus detectors are shown in Fig. 20; these composite images (each exposure 100 s) were acquired during commissioning activities without full waveform optimization.

#### 4.2.5 Palomar (III): EMCCD

A 2D-doped  $1\text{ k} \times 2\text{ k}$  EMCCD was processed for on-sky observation at Palomar. A single-layer AR coating designed for FIREBall-2 (see Sec. 4.1.5) was selected for this device in order to allow higher efficiency beyond the FIREBall narrowband response. Three observation runs at Palomar were completed with this detector behind the Cosmic Web Imager (CWI)<sup>83,84</sup> as part of an ongoing campaign to evaluate the detector's on-sky

performance and to obtain science data to set the stage for future space missions. The first of these runs was in November 2015, with follow up in spring and fall of 2016.<sup>77</sup> The detector was operated at  $-105^\circ\text{C}$ , 10 MHz, initially with the NUVU v.2 CCCP controller and the most recent run with the v.3. CWI is an integral field spectrograph (IFS) with 24 slices that cover a  $60 \times 40\text{ arc sec}^2$  area with a resolution  $R \sim 5000$ . The EMCCD is significantly smaller than the normal CWI detector, and for these runs only half the field of view was observed (12 out of 24 slices, or  $30 \times 40\text{ arc sec}^2$ ). Results from these runs were compared to equivalent observations with the normal CWI detector. We compared both photon counting operation, at a range of gain values, and normal mode operation. The data gathering process has involved many short integrations on sky to track sky lines, and hence flexure during a long exposure; this will allow for higher resolution flexure correction. In addition, these runs were used to verify measured QE results using standard stars, in both normal mode and EM operation. Figure 21 shows the results of the second run at Palomar behind the CWI.

#### 4.3 Industry-Sponsored Efforts as Relevant to Space-Based Applications

A part of the innovation and development described here is highly leveraged by partnership and work with industry. The high-stability, high-durability, and high-efficiency response of 2D-doped silicon detectors has found applications in the semiconductor industry; a few examples are described below.

##### 4.3.1 Solar-blind APDs

One such project is collaboration between JPL, Radiation Monitoring Devices, Inc. (RMD), and Caltech (Prof. D. Hitlin)

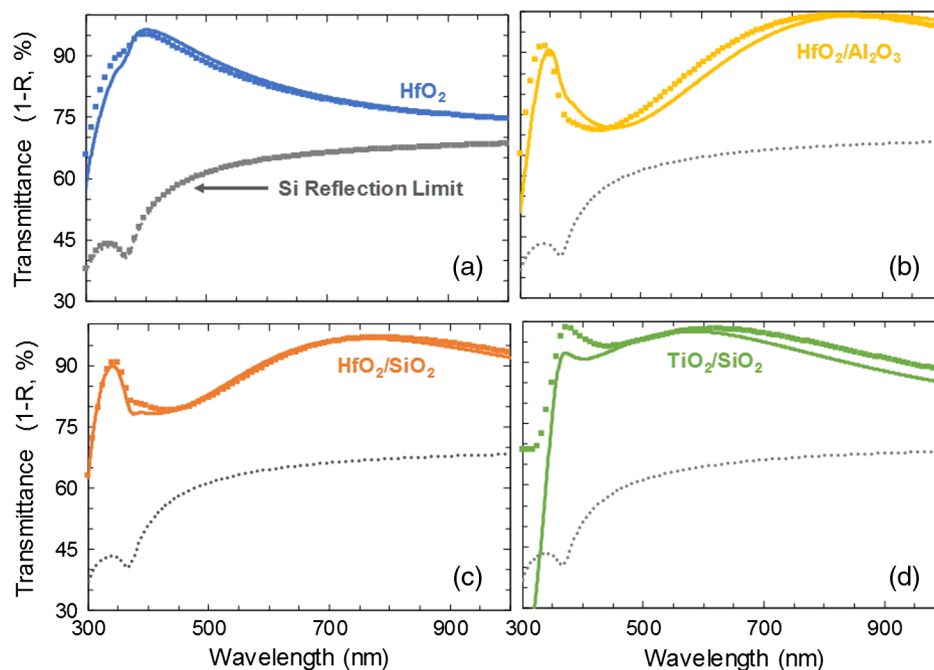


**Fig. 19** Model and measured transmittance data ( $100-R$ ) for WaSP/ZTF test samples (i.e., not test devices). The modeled transmittance data (solid lines) include expected losses due to reflection and absorption, whereas the measured data (square markers) were calculated based on sample reflectance only. Also shown is the reflection limited response for bare silicon (dotted line) together with a bare silicon reference sample (gray squares, upper left plot). Note samples A, B, and C each included a 2-nm  $d\text{-Al}_2\text{O}_3$ .<sup>82</sup>

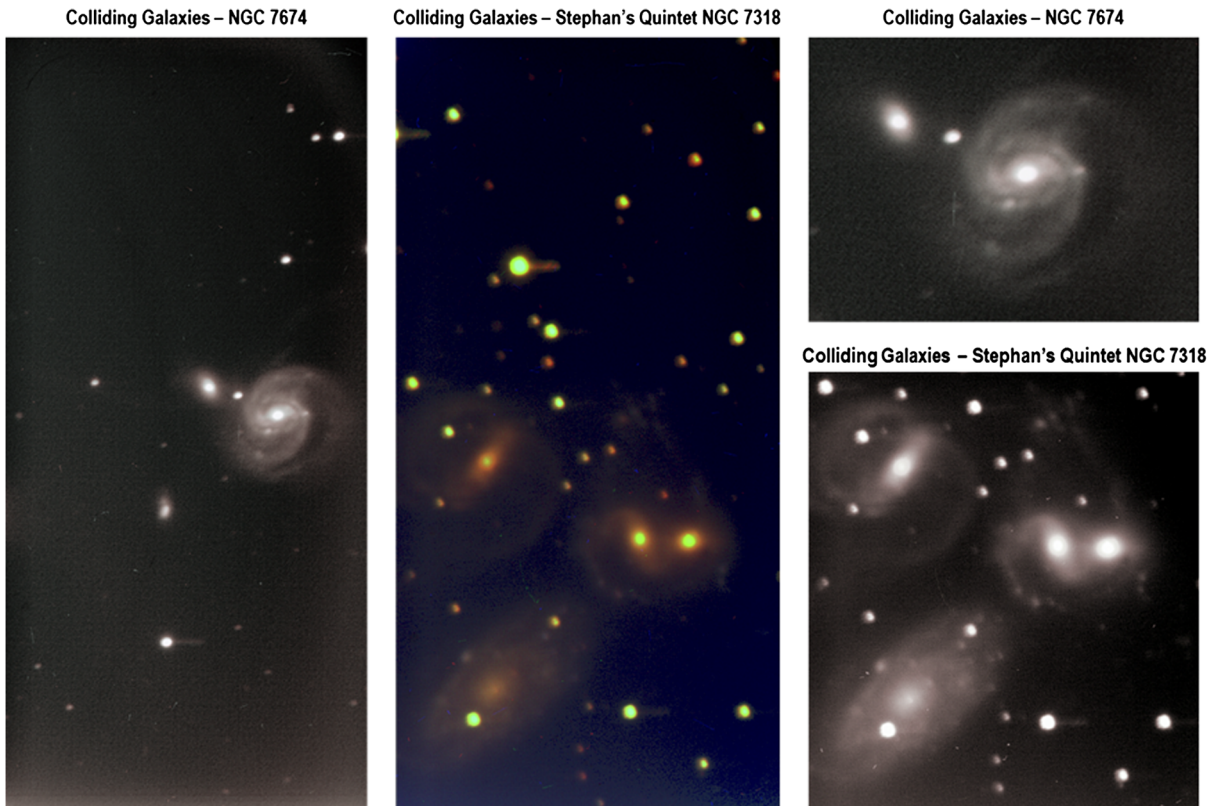


**Fig. 20** First light images from WaSP 2D-doped and AR-coated guide and focus detector. Shown are composite images comprised of 100-s exposures from the G', R', and U' bands (G', green; R', red; U', blue; color composite created with Photoshop CC 2017).

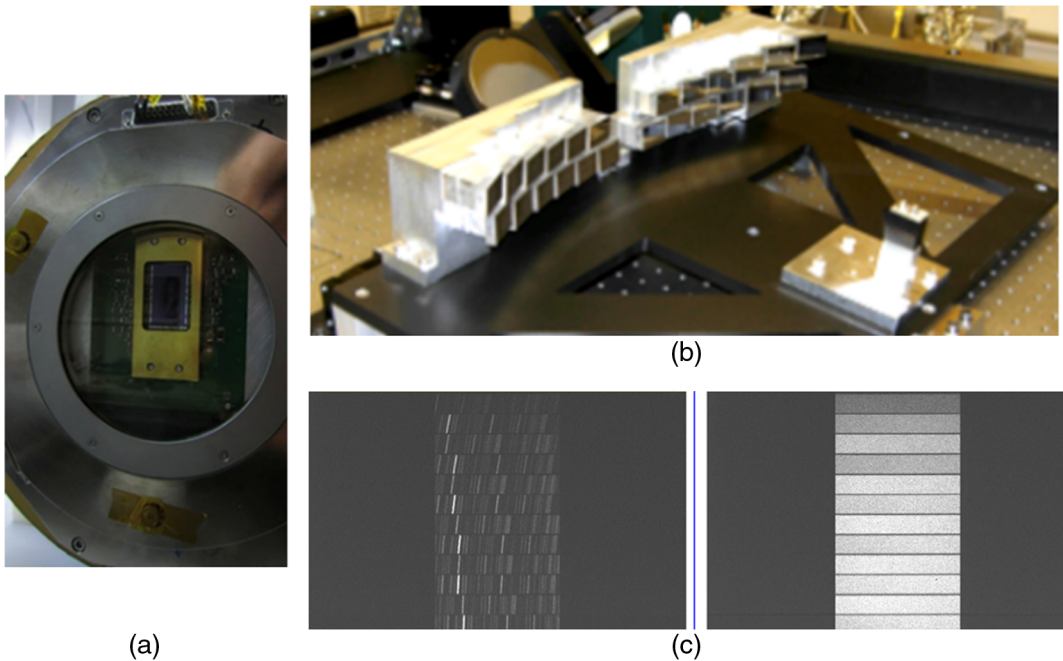


**Fig. 21** Photographs of (a) the FIREBall-2 detector prototype installed in the dewar for measurements at (b) CWI. (c) Test images acquired with the 2D-doped, AR-coated EMCCD from CWI. The tiled image shows arcflat and continuum flat images needed for calibration geometry. These 5-s exposures were acquired using the EM/gain function, which improves signal-to-noise and significantly shortens calibration time.

on the development of gamma ray scintillation detectors with subnanosecond temporal resolution and the capability to withstand unprecedented rates and doses of high-energy gamma radiation.<sup>85,86</sup> The system consists of doped BaF<sub>2</sub> scintillating crystals and solar-blind silicon APDs for detecting the fast scintillation component of BaF<sub>2</sub>. High efficiency and fast response are achieved by superlattice-doping of the APD. Integrated solar-blind MDFs enable efficient detection of the fast component of BaF<sub>2</sub> scintillation at 220 nm, with strong suppression of the slow component at 330 nm (Fig. 22). This work represents a significant move toward solar-blind silicon.

The ultrafast response time of these detectors is ideal for NASA applications such as x-ray pulsar navigation, time-gated Raman spectroscopy, and planetary gamma ray spectrometers. NASA has flown a number of instruments and missions using scintillation detectors, including MESSENGER's Gamma ray and neutron spectrometer; the CGRO Energetic Gamma Ray Experiment Telescope (CGRO/EGRET); the Fermi Large Area Telescope (Fermi/LAT); and the Fermi Gamma-Ray Burst Monitor (Fermi/GBM). The unique capabilities of this subnanosecond scintillation detector are an enabling technology for NASA's Advanced Compton Telescope and other missions requiring high-efficiency gamma-ray detection with excellent time resolution, such as a follow-on to the Fermi/LAT.

#### 4.3.2 Ultrastable CMOS imagers

Many scientific and commercial detectors are exposed to ionizing radiation. In such environments, detectors can rapidly lose sensitivity, develop instabilities, and in extreme cases, cease to function altogether. One such application is wafer and reticle inspection in semiconductor foundries. As the industry has progressed toward higher density circuits, state-of-the-art metrology systems have evolved to use pulsed, deep ultraviolet (DUV) lasers for optical detection of defects on the size scale of tens of nanometers. Unfortunately, state-of-the-art detectors degrade rapidly under intense illumination with DUV lasers. To address this challenge, JPL and Alacron have developed a high-performance, DUV camera with a superlattice-doped 3.2-megapixel CMOS imaging detector. Superlattice-doped detectors are uniquely stable against surface damage caused by DUV photons, as demonstrated by lifetime tests comprising exposure to pulsed, DUV lasers at 263 and 193 nm. Superlattice-doped CMOS imaging detectors survived long-term exposure to more than two billion laser pulses with no measurable degradation, no blooming, and no persistence. Additional details regarding this work are available in Ref. 39. The stability demonstrated with the 2D-doped CMOS platform has immediate application in precision photometry for astrophysics and cosmology. Our current focus on 2D-doped, low-noise CMOS will build on the work presented here to benefit future space missions.

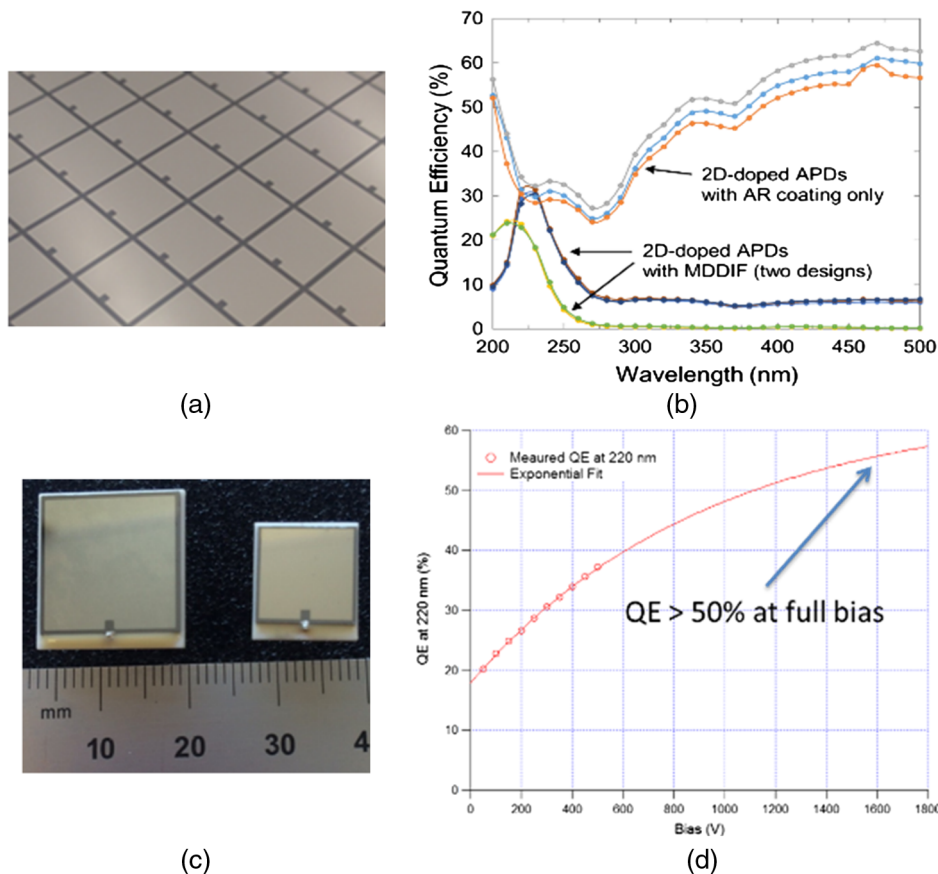


**Fig. 22** (a) Close-up view of a fully processed APD wafer following superlattice doping and the deposition/patterning of the MDF. (b) Response of 2D-doped APDs with alternate integrated MDF designs for the 200- to 240-nm range show comparable in-band QE and good out-of-band rejection compared to devices with AR coating only. (c) Packaged APDs of different sizes. (d) The QE at 220 nm plotted as a function of bias voltage for a 2D-doped APD with integrated MDF.

#### 4.4 Satellite Deployment

The end-to-end postfabrication processing, which includes 2D passivation, has been applied to a variety of device designs and formats. These devices have been extensively characterized by various groups and laboratories and have been deployed in suborbital experiments and observatories. Examples of orbital satellite missions that are using these devices in their baseline design are described here.

##### 4.4.1 Mission of Opportunity: ULTRASAT

The Ultraviolet Transient Astronomy Satellite (ULTRASAT) is a Partnership Mission of Opportunity concept that will further our understanding of the transient UV sky. ULTRASAT will undertake a wide-field UV time-domain survey of the sky and provide NUV light curves for hundreds of young supernovae. Both WaSP and ZTF (Sec. 4.2.4) serve as science pathfinders for ULTRASAT, as they will be performing similar measurements, albeit in a different portion of the spectrum. An additional goal of ULTRASAT is to constrain the physics of the sources of gravitational waves through a search for UV emission from a large sample of events. ULTRASAT is unique in its capability to rapidly observe a large fraction of the sky with its large field of view for sky localization of GW sources. This enables ULTRASAT to detect or constrain UV emission from neutron star mergers.

In order to achieve its objectives, ULTRASAT requires a large field of view, high-sampling cadence and high sensitivity. The ULTRASAT payload consists of a modified Schmidt telescope and a UV camera (ULTRACam) together providing a  $>210 \text{ deg}^2$  field of view and 21.3 AB limiting magnitude in the ULTRASAT band (220 to 280 nm). The ULTRACam focal plane is a 40-megapixel mosaic of five 2D-doped and AR-coated  $2 \text{ k} \times 4 \text{ k}$  CCDs (e2v CCD 42-80) optimized for NUV. The response of the prototype ULTRASAT detector exhibits peak QE  $> 75\%$ , shown for the first time here [Fig. 23(b)]. Work on the WaSP/ZTF and FIREBall-2 projects serves as technology pathfinders for the ULTRACam detector.

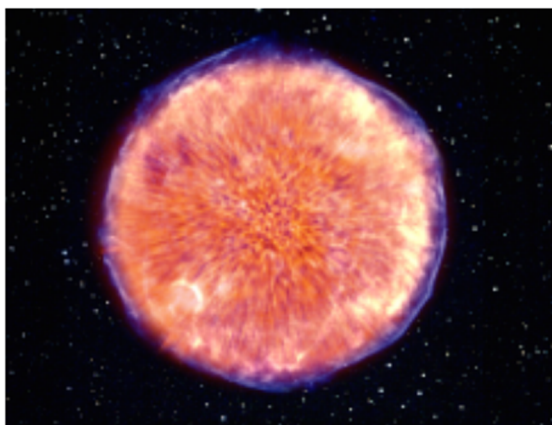
##### 4.4.2 Explorer class mission: mapping the circumgalactic and intergalactic media

An Explorer-class mission concept is currently under development that will map Lyman- $\alpha$  and metal emission lines from the CGM of low redshift galaxies, similar to the narrower search conducted by FIREBall-2 but over a larger wavelength range. The satellite will use a wide-field UV imaging spectrometer, and the mission has baselined an array of delta-doped EMCCDs for a two channel UV IFS (NUV and FUV). These observations will link the evolution of galaxies and star formation through cosmic time with the evolution of gas flows into and out of the CGM and IGM. The primary goal is to explain the dramatic evolution of cosmic star formation in the modern age and the formation of the galaxies we see today. The mission will survey the CGM in emission, characterizing a reservoir of the majority of the baryons in the universe. It will search for emission from the general IGM in deep observations. UV capability is required for these observations because most emission is in rest-frame UV lines that are only observable below  $z = 1.5$  in the space UV. In addition, the UV sky is very dark, making observations easier. The focal plane consists of an array of detectors with customized AR-coatings dictated by their spectral position in the array, covering 120 to 350 nm between the two channels. In the past several years, we have demonstrated  $>50\%$  QE over individual bands throughout the 120- to 300-nm range (Fig. 24). Our work on the FIREBall-2 mission serves as a pathfinder for both the CGM/IGM science as well as the detector technology (i.e., the 2D-doped and AR-coated EMCCD).<sup>78,79,81</sup>

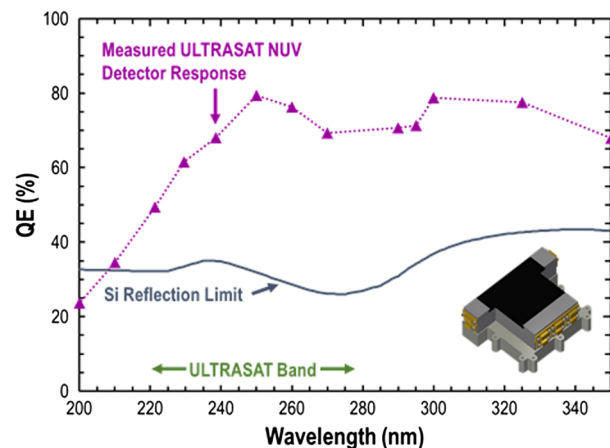
#### 4.5 Looking to the Future

##### 4.5.1 Probe class mission: ANUBIS

The Astronomical UV Probe Imager Spectrograph (ANUBIS) is a Probe-class UV-Optical Space Observatory currently in the formulation phase. The initial mission concept for ANUBIS combines a wide-field UV-optical imager with a FUV spectrograph. This next generation observatory will be capable of



(a)



(b)

**Fig. 23** (a) One of the ULTRASAT's objectives is to study the death of massive stars. Shown in violet is the shock breakout of the star, which is expected to shine strongly in the UV. (b) Plots showing the measured QE for the ULTRASAT NUV detector (purple triangles, dotted line), a 2D-doped and AR-coated detector. The plotted data have been QY corrected. Also shown is the silicon reflection limit, that is, the response of a non-AR-coated, 2D-doped CCD. Inset: concept of the ULTRASAT focal plane with a mosaic of five  $2 \text{ k} \times 4 \text{ k}$  CCDs.

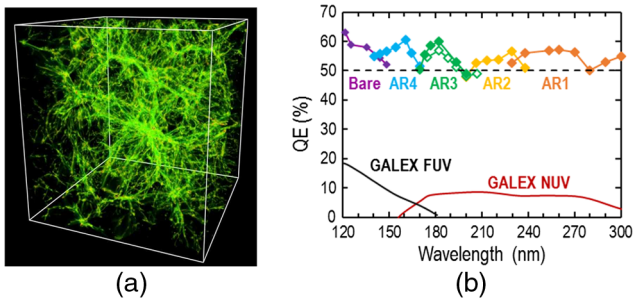


**Fig. 24** (a) Studies of CGM/IGM will shed light on the evolution of galaxies and star formation through cosmic time. (b) Early efforts for this mission have demonstrated >50% QE throughout the spectral range of interest using AR-coated, 2D-doped detectors. For this work, each spectral region was targeted using a customized AR coating. Both conventional CCDs (closed diamonds) and EMCCDs (open diamonds) were used in this work.<sup>61</sup> Responses of the GALEX MCP detectors are shown for comparison.<sup>87,88</sup>

conducting wide-field imaging surveys to study the formation and survival of stellar and planet forming environments. ANUBIS will include a FUV spectrograph with the wavelength coverage to reach the forest of diagnostic emission and absorption lines necessary to study the interface between galaxies and the intergalactic medium, to probe the structure and dynamics of the ISM in all its phases, both locally and in extragalactic systems.

Imaging surveys of large angular areas are necessary to conduct assays of widely scattered populations of objects—requiring large angular area coverage to locate the sources and high angular resolution to characterize sources once found. To maximize survey efficiency, multiple imaging channels are needed, fed by dichroics, and each focal plane must be optimized for its particular passband. This requires the production of large numbers of detectors, as well as the capability to tune the response of the detector to specific passbands.

ANUBIS employs a dichroic design with two large-area focal plane arrays (FPAs), splitting the spectral range into “blue” (210 to 510 nm) and “red” (500 to 1000 nm) channels. To achieve the highest QE in this range, ANUBIS baselines JPL’s 2D doping in combination with high-purity CCD arrays. Two different AR coatings are designed to cover the blue and

red channels of ANUBIS (Fig. 25). A collaborative JPL-ASU effort has demonstrated the QE for these two channels. In addition to the high QE, photometric stability that is provided by the 2D doping is essential for achieving ANUBIS objectives.

Additionally, 2D-doped EMCCDs can be optimized for the ANUBIS FUV spectrograph, offering photon counting and high UV efficiency.

#### 4.5.2 LUVOIR and HabEx

NASA is currently studying four flagship-class mission concepts as input to the 2020 National Research Council Decadal Survey on Astronomy and Astrophysics. Two of those mission concepts involve the use of the UV-optical passbands to address both general astrophysics and exoplanet direct imaging. LUVOIR is currently being conceived as either a 9- or 15-m aperture segmented telescope, whereas HabEx is being considered as either a 4-m monolith or a 6.5-m segmented telescope. (At the time of submission of this paper, both LUVOIR and HabEx are in the concept phases of development; it is likely that the configuration will evolve/change as these mission concepts mature.) In both cases, wide-field imagers are being baselined as foundational instruments together with FUV spectrographs to address the general astrophysics science goals of each mission concept.

In the case of the wide-field imager designs being formulated, the instrument calls for a large number of pixels to adequately sample the point spread function of the telescope, while providing enough discovery space ( $\Delta\Omega$ ) to perform efficient surveys in combination with characterization and analysis. The mirror coatings being considered will provide high reflectivity down to 200 nm; thus, the detectors chosen will need to deliver an optimum performance across the 200- to 1000-nm passband, with some possibility of dichroic splits to maximize efficiency. To this end, detector technologies will be needed that can be treated to deliver the needed response with a minimal level of risk. The 2D-doped, high-resistivity detectors delivered for WaSP/ZTF and CHESS, as well as those baselined for ANUBIS, provide the required spectral sensitivity in a proven platform.

The FUV spectrographs will similarly likely require large focal planes due to the need to provide a multiobject spectroscopic capability; this will likely require FPAs measured in the tens of centimeters. Detectors sensitive from the NUV (300 nm) down as low as 90 nm, depending on the mirror coating choices

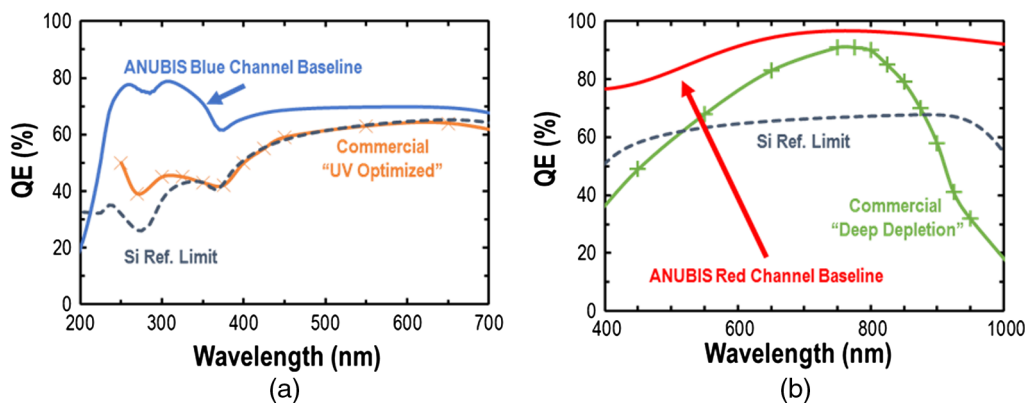


**Fig. 25** The QE models for ANUBIS (a) blue and (b) red channels. For comparison, the QE of commercially available UV-optimized (orange) and deep depletion (green) CCDs are also plotted, as is the silicon reflection limit (gray).

made, will be required. The selected focal plane technologies will need to deliver an efficient response across that passband at a resolution element pitch of probably 10 to 20  $\mu\text{m}$  in size. The FUV-optimized, 2D-doped detectors that have been delivered for various suborbital missions, including FIREBall-2, as well as those under development for ULTRASAT, the CGM/IGM Mapper, and ANUBIS, are ideal candidates.

The promise of these next generation mission concepts is staggering when compared with modern facilities even in the 30-m class being considered for the ground, so the detectors chosen to baseline the performance will need to represent the very best and most cutting-edge technologies the community can provide. As such to be eligible for adoption, the requisite technologies will need to demonstrate TRL 6 or 7 performance by the end of phase A which we expect to be no earlier than 2024, assuming WFIRST-AFTA is launched as projected. The development and deployment of high-performance 2D-doped silicon arrays described here put us in a strong position for the future.

## 5 Conclusions

We have presented an overview of the development of high-efficiency silicon detectors: from technology invention to laboratory demonstration of the first delta-doped array, and on to today's 2D-doped, 12-megapixel arrays and multiple arrays produced using our high-throughput processing. We have shown a survey of deployment of these 2D-doped detectors in space- and ground-based experiments and observatories. Along the way, major milestones in UV/optical/NIR band have been demonstrated, including, but not limited to, high QE in n-channel and p-channel silicon arrays; 2D-doped, high QE EMCCDs and CMOS arrays; and detector-integrated filters with out-of-band rejection ratios rivaling those of microchannel plates but with higher in-band efficiency. Adding to that, the scaled-up manufacturing of these detectors allows population of large FPAs foreseen for the next generation of space telescopes, such as LUVOIR and HabEx.

## Acknowledgments

The research was carried out in part at the Jet Propulsion Laboratory, California Institute of Technology, under a contract with the National Aeronautics and Space Administration. The authors gratefully acknowledge the support from NASA-SAT, NASA-APRA, JPL RTD program, the Keck Institute for Space Studies, and many years of other support from NASA and JPL and other agencies. E.T.K. acknowledges the support by Nancy Grace Roman Fellowship, the Millikan Prize in Experimental Physics, and the NSF Fellowship. The authors would like to acknowledge generous and excellent collaborative support from e2v including A. Reinheimer, P. Jerram, P. Pool, P. Jorden, and P. Fochi on the 2D-doped EMCCDs. The authors gratefully acknowledge the collaborative work with LBNL. S. Holland, C. Bebek, N. Roe, and their team that has led to the demonstration and development of 2D-doped, p-channel CCDs; as well as Bruno Milliard and Robert Grange of LAM for the FIREBall-2 spectrograph data. We acknowledge M. McClish of RMD for APD QE data and wafer processing. We also thank S. R. Kulkarni, R. Smith, and J. Milburn of Caltech Optical Observatories and Palomar Observatory for WaSP delta-doped array first-light images; as well as R. Goldstein and team for the MICA-LEES flight.

## References

1. R. D. Blandford et al., *New Worlds, New Horizons in Astronomy and Astrophysics*, The National Academies Press, Washington, DC (2010).
2. S. R. Shortes et al., "Characteristics of thinned backside-illuminated charge-coupled device imagers," *Appl. Phys. Lett.* **24**(11), 565–567 (1974).
3. M. M. Blouke et al., "Ultraviolet downconverting phosphor for use with silicon CCD imagers," *Appl. Opt.* **19**(19), 3318–3321 (1980).
4. J. T. Trauger, "Sensors for the Hubble space telescope wide field and planetary cameras (1 and 2)," in *CCDs Astron. Proc. Conf.*, Tucson, AZ, Sept. 6–8, 1989, pp. 217–230, Astronomical Society of the Pacific, San Francisco (1990).
5. J. R. Janesick, *Scientific Charge-Coupled Devices*, SPIE Press, Bellingham (2001).
6. M. E. Hoenk et al., "Growth of a delta-doped silicon layer by molecular beam epitaxy on a charge-coupled device for reflection-limited ultraviolet quantum efficiency," *Appl. Phys. Lett.* **61**(9), 1084–1086 (1992).
7. J. M. Jenkins et al., "High precision photometry with back-illuminated CCDs," *ASP Conf. Ser.* **119**, 277–280 (1997).
8. M. J. S. Belton et al., "The Galileo solid-state imaging experiment," *Space Sci. Rev.* **60**, 413–455 (1992).
9. M. Clampin, "WFPC-II CCDs," *WFPC-II ISR 2-06* (1992).
10. H. Bushouse, "WFC3 TV3 testing: UVIS science monitor," Instrument Science Report WFC3 2008–37 (2008).
11. M. H. Wong et al., "Overview of the WFC3 cycle 17 detector monitoring campaign," Instrument Science Report WFC3 2009–07 (2009).
12. S. Nikzad et al., "Digital imaging for planetary exploration," in *Handbook of Digital Imaging*, M. Kriss, Ed., Wiley, New York (2015).
13. P. J. W. Noble, "Self-scanned silicon image detector arrays," *IEEE Trans. Electron Devices* **15**(4), 202–209 (1968).
14. E. R. Fossum, "Active pixel sensors: are CCD's dinosaurs?" *Proc. SPIE* **1900**, 2 (1993).
15. E. R. Fossum, "CMOS image sensors: electronic camera-on-a-chip," *IEEE Trans. Electron Devices* **44**(10), 1689–1698 (1997).
16. J. Janesick, J. T. Andrews, and T. Elliott, "Fundamental performance differences between CMOS and CCD imagers: part I," *Proc. SPIE* **6276**, 62760M (2006).
17. J. Janesick et al., "Fundamental performance differences between CMOS and CCD imagers: part II," *Proc. SPIE* **6690**, 669003 (2007).
18. P. Magnan, "Detection of visible photons in CCD and CMOS: a comparative view," *Nucl. Instrum. Methods Phys. Res. Sect. A* **504**(1–3), 199–212 (2003).
19. S. E. Holland et al., "Fabrication of back-illuminated, fully depleted charge-coupled devices," *Nucl. Instrum. Methods Phys. Res. Sect. A* **579**(2), 653–657 (2007).
20. M. Lesser and D. Ouellette, "Development of hybridized focal plane technologies," *Proc. SPIE* **6276**, 627603 (2006).
21. Y. Bai et al., "Teledyne imaging sensors: silicon CMOS imaging technologies for x-ray, UV, visible, and near infrared," *Proc. SPIE* **7021**, 702106 (2008).
22. L. J. Kozlowski et al., "Large area visible arrays: performance of hybrid and monolithic alternatives," *Proc. SPIE* **4836**, 247 (2002).
23. E. Charbon et al., "SPAD-based sensors," in *TOF Range-Imaging Cameras*, F. Remondino and D. Stoppa, Eds., pp. 11–38, Springer, Heidelberg (2013).
24. C. Veerappan, Y. Maruyama, and E. Charbon, "Silicon integrated electrical micro-lens for CMOS SPADs based on avalanche propagation phenomenon," in *Int. Image Sensor Workshop*, Snowbird, Utah, USA (2013).
25. C. Niclass et al., "A 128 × 128 single-photon image sensor with column-level 10-bit time-to-digital converter array," *IEEE J. Solid-State Circuits* **43**(12), 2977–2989 (2008).
26. M. E. Hoenk et al., "Delta-doped back-illuminated CMOS imaging arrays: progress and prospects," *Proc. SPIE* **7419**, 74190T (2009).
27. P. F. Morrissey, S. R. McCandliss, and P. D. Feldman, "Vacuum-ultraviolet quantum efficiency of a thinned, backside-illuminated charge-coupled device," *Appl. Opt.* **34**(22), 4640 (1995).
28. R. Winzenread et al., "Improved uniformity in thinned scientific CCDs," *Proc. SPIE* **1161**, 67 (1989).
29. R. Winzenread, "Flat, thinned scientific CCDs," *Proc. SPIE* **2198**, 886 (1994).
30. S. Nikzad et al., "Delta-doped CCDs: high QE with long-term stability at UV and visible wavelengths," *Proc. SPIE* **2198**, 907 (1994).

31. T. J. Jones et al., "Thinned charge coupled devices with flat focal planes for UV imaging," *Proc. SPIE* **3965**, 148 (2000).
32. Q.-Y. Tong, G. G. Fountain, Jr., and P. M. Enquist, "Method for low temperature bonding and bonded structure," U.S. Patent No. 6902897 (2005).
33. S. Nikzad et al., "Single photon counting UV solar-blind detectors using silicon and III-nitride materials," *Sensors* **16**(6), 927–947 (2016).
34. K. Rajkanan, R. Singh, and J. Shewchun "Absorption coefficient of silicon for solar cell calculations," *Solid-State Electron.* **22**(9), 793–795 (1979).
35. J.-M. Defise, J. D. Moses, and F. Clette, "In-orbit performances of the EIT instrument on board SOHO and intercalibration with the EIT Calroc Sounding Rocket program," *Proc. SPIE* **3442**, 126 (1998).
36. M. E. Hoenk et al., "Superlattice-doped silicon detectors: progress and prospects," *Proc. SPIE* **9154**, 915413 (2014).
37. S. Nikzad et al., "Ultrastable and uniform EUV and UV detectors," *Proc. SPIE* **4139**, 250 (2000).
38. M. E. Hoenk et al., "Epitaxial growth of p+ silicon on a backside-thinned CCD for enhanced UV response," *Proc. SPIE* **1656**, 488 (1992).
39. M. E. Hoenk et al., "The DUV stability of superlattice-doped CMOS detector arrays," in *Int. Image Sensor Workshop*, Snowbird, Utah, USA (2013).
40. M. E. Hoenk, "Surface passivation by quantum exclusion using multiple layers," U.S. Patent No. 8,395,243 (2013).
41. J. Blacksberg et al., "Enhanced quantum efficiency of high-purity silicon imaging detectors by ultralow temperature surface modification using Sb doping," *Appl. Phys. Lett.* **87**(25), 254101 (2005).
42. J. Blacksberg, M. E. Hoenk, and S. Nikzad, "Ultra-low-temperature homoepitaxial growth of Sb-doped silicon," *J. Cryst. Growth* **285**(4), 473–480 (2005).
43. R. C. Jaeger, *Introduction to Microelectronic Fabrication*, Addison-Wesley Publishing Company, New York (1993).
44. P. H. Citrin et al., "Breaking through the electrical saturation barrier: 2D-versus 3D-doping in n-type silicon," *Physica B: Condens. Matter* **273–274**, 251–255 (1999).
45. R. L. Headrick et al., "Si(100)-(2×1) boron reconstruction: self-limiting monolayer doping," *Appl. Phys. Lett.* **57**(26), 2779–2781 (1990).
46. M. Lesser, "Antireflection coatings for silicon charge-coupled devices," *Opt. Eng.* **26**(9), 269911 (1987).
47. E. T. Hamden et al., "Ultraviolet antireflection coatings for use in silicon detector design," *Appl. Opt.* **50**(21), 4180–4188 (2011).
48. S. M. George, "Atomic layer deposition: an overview," *Chem. Rev.* **110**(1), 111–131 (2010).
49. I. Heyer et al., *WFPC2 Instrument Handbook (August)*, Version 9, STScI, Baltimore (2004).
50. Acton Optics, "VUV/UV notch-reflective filters," <http://www.actonoptics.com/products/notch-filters> (4 April 2017).
51. M. Zukic et al., "Filters for the international solar-terrestrial physics mission far-ultraviolet imager," *Opt. Eng.* **32**(12), 3069–3074 (1993).
52. S. E. Tuttle et al., "FIREBALL: the first ultraviolet fiber fed spectrograph," *Proc. SPIE* **7732**, 773227 (2010).
53. J. Hennessy et al., "Metal-dielectric filters for solar-blind silicon ultraviolet detectors," *Appl. Opt.* **54**(11), 3507–3512 (2015).
54. M. Putkonen et al., "Thermal and plasma enhanced atomic layer deposition of SiO<sub>2</sub> using commercial silicon precursors," *Thin Solid Films* **558**, 93–98 (2014).
55. J. Hennessy et al., "Performance and prospects of far ultraviolet aluminum mirrors protected by atomic layer deposition," *J. Astron. Telesc. Instrum. Syst.* **2**(4), 041206 (2016).
56. "TFCalc: thin film design software for windows," Version 3.5, Software Spectra, Inc., (2009).
57. E. D. Palik, Ed., *Handbook of Optical Constants of Solids*, Academic Press, San Diego (1998).
58. S. Nikzad et al., "High performance silicon imaging arrays for cosmology, planetary sciences, & other applications," in *IEEE Int. Electron Devices Meeting*, pp. 10.7.1–10.7.4, IEEE, San Francisco (2014).
59. V. S. Argabright et al., "The Kepler photometer focal plane array," *Proc. SPIE* **7010**, 70102L (2008).
60. J. H. J. de Bruijne, "Science performance of Gaia, ESA's space-astrometry mission," *Astrophys. Space Sci.* **341**(1), 31–41 (2012).
61. S. Nikzad et al., "Delta doped electron multiplies CCD with absolute quantum efficiency over 50% in the near to far ultraviolet range for single photon counting applications," *Appl. Opt.* **51**(3), 365–369 (2012).
62. J. Trauger, "JPL internal report," (1996).
63. J. Blacksberg et al., "Near-100% quantum efficiency of delta doped large-format UV-NIR silicon imagers," *IEEE Trans. Electron Devices* **55**(12), 3402–3406 (2008).
64. F. Greer et al., "Atomically precise surface engineering of silicon CCDs for enhanced UV quantum efficiency," *J. Vac. Sci. Technol. A* **31**(1), 01A103 (2013).
65. J. M. Owens and E. L. Riddle, "Big science on a small budget: a university sounding rocket," in *11th Annual AIAA/Utah State University Conf. on Small Satellites*, Logan, Utah, pp. 1–15, (1997).
66. S. R. McCandliss et al., "Long-slit imaging dual-order spectrograph: LIDOS," *Proc. SPIE* **4854**, 385 (2003).
67. R. E. Lupu et al., "Calibration and flight performance of the long-slit imaging dual order spectrograph," *Proc. SPIE* **7011**, 70113I (2008).
68. K. France et al., "Rocket and far ultraviolet spectroscopic explorer observations of IC 405: differential extinction and fluorescent molecular hydrogen," *Astrophys. J.* **616**(1), 257–265 (2004).
69. K. France and S. R. McCandliss, "Molecular hydrogen in orion as observed by the far ultraviolet spectroscopic explorer," *Astrophys. J.* **629**(2), L97–L100 (2005).
70. S. Nikzad et al., "Direct detection of 0.1-20 keV electrons with delta doped, fully depleted, high purity silicon p-i-n diode arrays," *Appl. Phys. Lett.* **89**(18), 182114 (2006).
71. K. France et al., "Development of the Colorado High-resolution Echelle Stellar Spectrograph (CHESS)," *Proc. SPIE* **8443**, 844305 (2012).
72. K. Hoadley et al., "The assembly, calibration, and preliminary results from the Colorado High-resolution Echelle stellar Spectrograph (CHESS)," *Proc. SPIE* **9144**, 914406 (2014).
73. K. France, B. Fleming, and K. Hoadley, "CHISL: the combined high-resolution and imaging spectrograph for the LUVUOIR surveyor," *Proc. SPIE* **9905**, 990506 (2016).
74. S. Redfield, "The local interstellar medium," in *ASP Conf. Series 352, Frank N. Bash Symposium 2005: New Horizons in Astronomy*, Vol. **352** (2006).
75. K. Hoadley et al., "The re-flight of the Colorado High-resolution Echelle Stellar Spectrograph (CHESS): improvements, calibrations, and post-flight results," *Proc. SPIE* **9905**, 99052V (2016).
76. B. Milliard et al., "FIREBALL: the faint intergalactic medium red-shifted emission balloon: overview and first science flight results," *Proc. SPIE* **7732**, 773205 (2010).
77. G. Kyne et al., "The faint intergalactic-medium red-shifted emission balloon: future UV observations with EMCCDs," *Proc. SPIE* **9915**, 991507 (2016).
78. A. D. Jewell et al., "Detector performance for the FIREBall-2 UV experiment," *Proc. SPIE* **9601**, 96010N (2015).
79. E. T. Hamden et al., "Noise and dark performance for FIREBall-2 EMCCD delta-doped CCD detector," *Proc. SPIE* **9601**, 96010O (2015).
80. P. Kuschnerus et al., "Characterization of photodiodes as transfer detector standards in the 120 nm to 600 nm spectral range," *Metrologia* **35**(4), 355–362 (2003).
81. E. T. Hamden et al., "Charge-coupled devices detectors with high quantum efficiency at UV wavelengths," *J. Astron. Telesc. Instrum. Syst.* **2**(3), 036003 (2016).
82. A. D. Jewell et al., "Wide band antireflection coatings deposited by atomic layer deposition," *Proc. SPIE* **8820**, 88200Z (2013).
83. M. Matuszewski et al., "The Cosmic Web Imager: an integral field spectrograph for the Hale Telescope at Palomar Observatory: instrument design and first results," *Proc. SPIE* **7735**, 77350P (2010).
84. P. Morrissey et al., "The Keck Cosmic Web Imager: a capable new integral field spectrograph for the W. M. Keck Observatory," *Proc. SPIE* **8446**, 844613 (2012).
85. D. G. D. Hitlin et al., "An APD for the detection of the fast scintillation component of BaF<sub>2</sub>," *IEEE Trans. Nucl. Sci.* **63**(2), 513–515 (2016).
86. D. G. Hitlin et al., "An APD for the efficient detection of the fast scintillation component of BaF<sub>2</sub>," *Nucl. Instrum. Methods Phys. Res. Sect. A* **824**, 119–122 (2016).
87. P. Jelinsky et al., "Performance results of the GALEX cross delay line detectors," *Proc. SPIE* **4854**, 233 (2003).
88. P. Morrissey, "A GALEX instrument overview and lessons learned," *Proc. SPIE* **6266**, 62660Y (2006).

**Shouleh Nikzad** is a senior research scientist, a principal engineer, lead for Advanced Detectors, Systems, and Nanoscience Group at NASA's Jet Propulsion Laboratory, and visiting faculty and lecturer at California Institute of Technology's Division of Physics, Math, and Astronomy as well as Medical Engineering Department. She has 15 US patents and near 100 publications. Her research interests are in materials and devices, development of detectors, instrument technologies, and instruments in ultraviolet/optical/near infrared. She is a fellow of SPIE.

**April D. Jewell** received her BS degree in chemistry from George Washington University and a PhD in chemistry from Tufts University. She is a technologist at the Jet Propulsion Laboratory. She has authored/coauthored more than 50 publications, including three book chapters. Her research interests include surface-level phenomena, advanced doping, and optical coatings.

**Michael E. Hoenk** is a principal microdevices engineer in the JPL's Flight Instrument Detectors Group, with extensive experience as principal investigator and leader of JPL research projects on imaging detectors, sensors, and instruments. His many inventions include delta-doped CCDs and superlattice-doped CMOS imaging detectors, which recently resulted in a breakthrough for semiconductor metrology systems. He has received many awards for his work, including the Lew Allen Award for Excellence and the NASA Exceptional Achievement Medal.

**Todd J. Jones** received his BS degree in physics from Harvey Mudd College with MS and PhD degrees in applied physics from Caltech. He is a microdevices engineer at the Jet Propulsion Laboratory. He has authored/coauthored more than 25 publications. His research interests include energetic particle detection, detector back illumination processes, and advanced detector packaging concepts.

**John Hennessy** received his BE degree from the Cooper Union in 2002 and his PhD degree from Massachusetts Institute of Technology in 2010, both in electrical engineering. He is a technologist at the Jet Propulsion Laboratory. His current research interests include the development of ALD processes for optical and electrical applications related to UV detector-integrated filters, UV reflective coatings, and semiconductor surface passivation.

**Tim Goodsall** is a technologist at the Jet Propulsion Laboratory specializing in the characterization and deployment of detectors and imaging arrays. He received his BA and MSc degrees in theoretical and experimental physics from Cambridge University and his DPhil in astrophysics from Oxford University, where he helped develop and deploy an integral-field-spectrograph for Palomar Observatory using a fully depleted p-channel CCD. He joined the Advanced Detectors, Systems, and Nanoscience Group in 2011 after completing a visiting scientist position supporting an Explorer Proposal.

**Alexander G. Carver** received his BS, MS, and PhD degrees in electrical engineering from Georgia Institute of Technology. He is a technologist at the Jet Propulsion Laboratory. His current work focuses on instrument system engineering utilizing developing technology as well as instrumentation and characterization design.

**Charles Shapiro** received a PhD in physics from the University of Chicago and a BS degree in math and physics from the Pennsylvania State University. He is a technologist at the Jet Propulsion Laboratory, where he transitioned from theoretical cosmology. His interests include characterization of large-format ultraviolet/visible/infrared detectors, especially understanding how detector nonidealities impact precision astronomy measurements such as photometry, astrometry, and shape measurement.

**Samuel R. Cheng** received his BS degree in electrical engineering and computer engineering from California State Polytechnic University and his MS degree in electrical engineering from the University of Southern California. He is an electronics engineer in the Advanced Detectors, Systems and Nanoscience Group, Jet Propulsion Laboratory, California Institute of Technology. His current research interests

are development of delta-doped detector hardware, detector characterization, development, and deployment; embedded software development, and special applications algorithm development.

**Erika T. Hamden** is an NSF astronomy and astrophysics postdoctoral fellow, the Caltech Millikan prize fellow in experimental astrophysics, and a Roman technology fellow at Caltech. She is an astrophysicist with degrees from Columbia University (PhD, 2014) and Harvard College (AB, 2006). Her work focuses on UV detector development and instrumentation, with a focus on detecting emission from the diffuse CGM of star forming galaxies. She is the project scientist for the FIREBall-2 mission.

**Gillian Kyne** received her PhD at the National University of Ireland, Galway in 2014. For the past two years, she has been a postdoctoral scholar at the California Institute of Technology. She is the detector scientist for the FIREBall-2 balloon mission, where her main role is characterizing the electron multiplying CCD noise and developing the camera that will fly for this mission. Her general interests lie in detector development for ground-based observing as well as future space based missions.

**D. Christopher Martin** is a professor of astrophysics at California Institute of Technology. He has been building astrophysics experiments for 37 years. He was the PI of NASA's Galaxy Evolution Explorer and is currently PI of the Keck Cosmic Web Imager and the FIREBALL-2 Balloon mission.

**David Schiminovich** is a professor of astronomy at Columbia University and a codirector of Columbia Astrophysics Laboratory. He received his BS degree in mathematics and physics from Yale University and his PhD from Columbia University. His research topics include galaxy formation and evolution, intergalactic and interstellar medium, and astronomical instrumentation. He served as a lead scientist on the Galaxy Evolution Explorer (GALEX) project, he is the institutional PI for the FIREBall-2 mission at Columbia, and he is a member of the LUVOR Science and Technology Definition Team

**Paul Scowen** is a research professor at the School of Earth and Space Exploration, Arizona State University. His interests include astrophysics space mission development, imaging, optomechanical and optoelectronic solutions for image stabilization, detectors, and next-generation mirror-coating technologies, star and planet formation in massive stellar environments. He has worked intimately with the Hubble Space Telescope and coauthored the iconic Eagle Nebula images and resulting papers. He serves on several NASA advisory committees and is an STDT member for the HabEx mission concept study.

**Kevin France** is a professor of astrophysics and planetary science at the University of Colorado. His research focuses on exoplanets and their host stars, protoplanetary disks, and the development of instrumentation for ultraviolet astrophysics. He is a regular guest observer with Hubble and is the PI of NASA-supported suborbital flight programs. He is a member of the LUVOR Science and Technology Definition Team and the instrument lead for the LUVOR UV spectrograph and imager.

**Stephan McCandliss** received his PhD in astrophysics from the University of Colorado, Boulder, in 1988. He is a research professor and director of the Center of Astrophysical Sciences at Johns Hopkins University. He has spent his entire postgraduate career developing innovative instrumentation for the purpose of carrying out spectroscopic and imaging observations of extended astronomical objects in the far-UV from sounding rocket borne experiments.

**Roxana E. Lupu** received her PhD from Johns Hopkins University in 2009, working on molecular fluorescence and far-UV instrumentation. She is a research scientist at BAER Institute/NASA Ames Research Center. Currently, her research focuses on atmospheric models and molecular opacity data for exoplanet characterization. As part of the science requirements team for the WFIRST coronagraph instrument, she develops inverse methods for interpreting reflected light spectra.